Time-averaging Polarimetric and Spectral Properties of GRBs

Liang Li[1,2,3]* Soroush Shakeri[4,1,5]†
[1]ICRANet, Piazza della Repubblica 10, I-65122 Pescara, Italy
[2]ICRA and Dipartimento di Fisica, Università di Roma "La Sapienza", Piazzale Aldo Moro 5, I-00185 Roma, Italy
[3]INAF – Osservatorio Astronomico d'Abruzzo, Via M. Maggini snc, I-64100, Teramo, Italy
[4]Department of Physics, Isfahan University of Technology, Isfahan 84156-83111
[5]ICRANet-Isfahan, Isfahan University of Technology, Isfahan 84156-83111, Iran

arXiv:2301.00576v1 [astro-ph.HE] 2 Jan 2023

Accepted XXX. Received YYY; in original form ZZZ

ABSTRACT

One of the most fundamental and yet open issues in gamma-ray burst (GRB) physics, is the comprehension of the nature of their jet composition. The investigation of joint polarimetric and spectral properties is essential to probe the jet composition and radiation mechanism of GRBs. Several distinct categories of jet properties—the "Kinetic-energy-dominated" (KED), "Poynting-flux-dominated" (PFD), and "Hybrid-dominated" (HD) jets—have been observed in the observed GRB spectra, and the emission dominated by different jet properties is expected to have a different level of polarization ($\pi_{\rm KED} \lesssim \pi_{\rm HD} \lesssim \pi_{\rm PED}$). In the present paper, we collected a GRB sample in which all the bursts detected by the Gamma-ray Burst Monitor (GBM) on board the NASA *Fermi* Gamma-ray Space Telescope whose polarization measurements are also reported in the literature and the epochs of prompt emission are heavily overlapped with their polarization observations, aiming to establish a connection between the polarization and jet properties of GRBs, and to confirm the validity of this correlation ($\pi_{\rm KED} \lesssim \pi_{\rm HD} \lesssim \pi_{\rm PED}$) from observations. With a detailed spectral analysis, we found that all the bursts are classified as the "Hybrid" jet type, implying that one cannot rule out that the photosphere emission may also be the possible mechanism powering the high levels of polarization. Moreover, we also discovered that the polarization degrees π are tightly correlated with the cosmological rest-frame peak energy ($E_{\rm p,z}$) of the νF_ν prompt emission spectrum, the isotropic-bolometric-equivalent emission energy ($E_{\gamma,\rm iso}$), and the blackbody temperature (kT). Finally, we present different polarization models in the presence of ordered and random magnetic field configurations with the properties of corresponding hybrid jets in order to interpret polarization measurements of the prompt emission in our sample.

Key words: gamma-ray burst: general, radiation mechanisms: non-thermal, radiation mechanisms: thermal

1 INTRODUCTION

Gamma-ray bursts (GRBs) are one of the most explosive, and electromagnetically the brightest transient phenomena in the Universe, occurrence at cosmological distances. After decades of investigation, the origin of the jet composition (a hot baryonic-dominated fireball or a cold Poynting-flux-dominated outflow), and the radiation mechanism and energy dissipation mechanism (synchrotron, or Comptonization of quasi-thermal emission from the photosphere) in gamma-ray burst (GRB) physics are still unclear (e.g., Rees & Meszaros 1994; Mészáros & Rees 2000; Rees & Mészáros 2005; Pe'er et al. 2006; Dai et al. 2006; Pe'er 2015; Pe'Er & Ryde 2017; Zhang 2018; Bégué et al. 2022).

There are two crucial clues that can in principle be helpful in diagnosing the jet composition of GRBs, as well as their radiation mechanism and energy dissipation mechanism. The conventional approach is to examine the spectral properties of prompt emission. Theoretically, a thermal component originating from photosphere emission, or a non-thermal component originating from synchrotron radiation, possibly also from inverse Compton scattering, is often expected to be present in GRB spectral analysis. Phenomenologically, GRB spectra in the keV-MeV energy range can be typically well-delineated by an empirical function, known as the Band function (Band et al. 1993), which is generally considered to be a non-thermal spectrum. The Band spectrum features a smoothly broken power law, with the peak energy $E_{\rm p} \simeq 210$ keV (the energy at which most of the energy is released) in $\nu F\nu$ space and the asymptotic power-law photon indices below ($\alpha \simeq -0.8$) and above ($\beta \simeq -2.5$) the break energy (e.g., Li et al. 2021). The low-energy spectra during GRB prompt emission phase are closely related to the energy distribution of electrons (e.g., Preece et al. 1998; Lloyd & Petrosian 2000; Geng et al. 2018). This fact can be utilized in order to diagnose GRBs radiation mechanism as well as their jet properties. For instance, synchrotron emission predicts two different α values: α=-3/2 and α=-2/3 (so-called the line-of-death (LOD) of synchrotron emission, Preece et al. 1998) correspond to the fast-cooling and slow-cooling synchrotron emission, respectively. It has been shown

* E-mail: liang.li@icranet.org (LL)
† E-mail:s.shakeri@iut.ac.ir (SS)

© 2023 The Authors

that the synchrotron emission in the presence of a decaying magnetic field can reproduce the Band-like spectrum of the GRB prompt phase (Lan et al. 2021). While photosphere models, on the other hand, predict much harder values of α; e.g., above α=-2/3. For example, a recent study (Acuner et al. 2020) suggests that the spectra that prefer the photospheric model all have low-energy power-law indices $\alpha \sim$>-0.5, as long as the data has a high significance. Years of observations have revealed, however, that GRBs have diverse spectral properties, making it difficult for a single spectral model (such as the Band-alone model) to accurately characterize all the spectral shapes. For instance, time-resolved and time-integrated spectral analysis inferred from the broadband *Fermi* observations have revealed that GRB prompt emission exhibits remarkably diverse spectral properties (e.g., Abdo et al. 2009; Ryde et al. 2010; Axelsson et al. 2012; Acuner et al. 2019; Li 2019a; Li et al. 2019, 2021, 2022b; Deng et al. 2022). A kinetic-energy-dominated (KED) jet characterised by a quasi-thermal Planck-like spectrum has been detected in some bursts (e.g. GRBs 090902B, 220426A, Ryde et al. 2010; Deng et al. 2022; Wang et al. 2022; Song et al. 2022), while a cold Poynting-flux-dominated (PFD) outflow characterised by a Band (or cutoff power-law[1])-only function (Band et al. 1993) has been also observed in some other bursts (e.g. GRB 080916C[2], GRB 130606B, and many others, Abdo et al. 2009; Li 2022a), even a hybrid-dominated (HD) relativistic outflow with a hot fireball component and a cold Poynting-flux component, characterized by either a composited spectral scenario, with a non-thermal component and a thermal component, e.g., GRBs 100724B, 110721A, 150314A, 190114C, and several others, Axelsson et al. 2012; Guiriec et al. 2011; Wang et al. 2019; Li 2022a; Li et al. 2022b), or a transition from a fireball to a Poynting-flux-dominated outflow within a single burst (e.g. GRBs 140206B, 160625B, and several others, Li 2019a), have also been observed.

An alternative approach is to investigate their polarization properties. Theoretically, photon polarizations play a key role to understand the jet composition, angular structure, geometric configuration, magnetic composition and magnetic field configuration of GRB jets, and radiation mechanism of GRB jets (Toma et al. 2009a; Lundman et al. 2013; Zhang 2014; Zhang et al. 2019). Although magnetic field configurations with relatively large coherence lengths more than gyroradius of charged particles can generate the same energy spectrum via synchrotron mechanism, the level of polarization may significantly different for various magnetic field structures. Therefore joint spectral and polarization analysis is essential to determine the magnetic field structure in outflow materials of GRBs (Granot 2003; Lyutikov et al. 2003; Granot & Königl 2003a; Kole et al. 2020). For instance, the center engine is anticipated to generate strong magnetic fields (a highly magnetized jet) and launch them concurrently with the relativistic jets. It is unclear, nevertheless, whether the GRB emission is caused by shock dissipation or magnetic reconnection, and whether the outflow is dominated by the photosphere or synchrotron emission (Toma et al. 2009a).

In fact, the generation of the polarization signal can be intrinsic to the emission process or due to the propagation effects Shakeri & Allahyari (2018). Several emission models (induced synchrotron emission, Rybicki & Lightman 1979; photosphere emission, Lundman et al. 2014a; and Compton drag model, Lazzati et al. 2004) have been proposed to explain the intrinsic polarization properties of relativistic jets during prompt emissions. (i) Synchrotron emission model. There are some studies (e.g., Rybicki & Lightman 1979; Toma et al. 2009b; Lan & Dai 2020) showing that higher values of linear polarized signal (polarization degree π ranging from 20% to 70%) is expected to be measured with an ordered magnetic field from the synchrotron emission from a relativistic jet. While jets with random magnetic fields produce lower levels of polarization, this is due to the polarization being canceled out so that the net polarization degree being close to zero for an on-axis observer. A polarization detection which is less than 15% is believed to be originated from a random magnetic field configuration within the jet (Mao & Wang 2013). For example, if the emission is dominated by the internal shock (IS) model, π is expected to range from 10% (the maxed magnetic field configuration) to 70% (the large-scale ordered magnetic field configuration). (ii) Dissipative photosphere model. The dissipative photosphere model predicts a relatively low degree of polarization in the γ-ray band. However, a structured jet photosphere model might also generate polarized photons by Compton scattering, but the degree of polarization would be energy-dependent from the synchrotron model in ordered magnetic fields. For instance, it is demonstrated that if the jet has considerable structure, the model may create polarizations of up to 40% within $\delta\Theta \sim \Gamma^{-1}$. However, in the absence of dissipation and below the photosphere the polarization is rather limited to values below 15%-20% (Gill et al. 2018). To restrict these models, a high-sensitivity gamma-ray polarimeter with a broad band-pass to detect energy-dependent polarization signals is required (Zhang 2014; Ito et al. 2014; Lundman et al. 2014a; Lundman et al. 2018a). (iii) Internal-collision-induced magnetic reconnection and turbulence (ICMART) model. In the ICMART model (Zhang & Yan 2011a), π is expected to range from 60 percent at the beginning of the pulse and down to about 10 percent at the end of the pulse. A decaying polarization degree is predicted.

It is highly speculated that the prompt emission is likely expected to be strongly polarized owing to its non-thermal origin (a non-thermal Band-like spectrum). Observationally, higher levels of linear polarization measured from prompt γ-ray emission have been reported by several authors (e.g., Coburn & Boggs 2003; Willis et al. 2005; McGlynn et al. 2007; Yonetoku et al. 2012a). For instance, a higher polarization degree $\pi = 80\% \pm 20\%$ in GRB 021006 was claimed by Coburn & Boggs (2003) using the RHESSI data. Later, several other cases were also reported, e.g., GRB 930131 ($\pi >$ 35%), GRB 960924 ($\pi >$ 50%), GRB 041219A, GRB 100826A ($\pi = 27\% \pm 11\%$), GRB 110301A ($\pi = 70\% \pm 22\%$), and GRB 110721A ($\pi = 84\%^{+16\%}_{-28\%}$). Subsequent observations were also observed in the optical band during the afterglow emission and were of relatively low polarization. Compared with prompt γ-ray emission, the levels of linear polarization measured from afterglow emission are relatively lower. e.g., GRB 060418 ($\pi <$ 8%), GRB 090102 ($\pi = 10.1\% \pm 1.3\%$), GRB 091208B ($\pi = 10.4\% \pm 2.5\%$), and 120328A ($\pi = 28\% \pm 4\%$). However, higher degrees of polarization observations are still expected to be measured from early reverse shocks, up to $\sim$ 60%.

Generally speaking, we can study GRB polarization and spectral properties either in a time-integrated (e.g., Li 2022a) or time-resolved (e.g., Li et al. 2021) manner. The former represents average polarimetric and spectral properties and is treated as a single-time event for the entire emission period. The latter treats the entire emission period as divided into multiple-time events, and polarimetric

[1] Recent studies (Li 2022b,a) supported by several pieces of additional evidence (e.g., inconsistent spectral parameter distributions and distinct Amati and Yonetoku correlations) have shown that Band-like spectra and CPL-like spectra may originate from distinct radiation processes.

[2] It has been demonstrated in recent studies (Guiriec et al. 2015; Vereshchagin et al. 2022) that a thermal component needs to be added during the initial prompt emission of GRB 080916C to obtain an acceptable fit to the spectral data.

and spectral analyses are therefore performed on each event individually. The time-integrated method depends more heavily on the statistical results of a large sample in order to produce a more trustworthy result because different bursts have distinct observational properties (e.g., angular structure). However, this issue does not arise when a time-resolved technique is used in the same burst since it ensures that other conditions (e.g., magnetic field configuration) are essentially the same and, therefore, makes it easier to obtain reliable results.

Following these lines of argument, the emissions dominated by different jet properties (KED, PFD, and HD) may have different levels of prompt-GRB polarization measurements[3] (Li 2019a). As a result, a different level of polarization degrees ($\pi_{\rm KED} \lesssim \pi_{\rm HD} \lesssim \pi_{\rm PED}$) is naturally expected due to different jet properties if other conditions are basically the same, where $\pi_{\rm KED}$, $\pi_{\rm HD}$, and $\pi_{\rm PED}$ are the polarization degree in the KED, HD, and PHD jets, respectively. This may provide a method to study the correlations between polarization properties and their spectral properties, as well as their jet properties. A possible connection between the spectral and polarization properties has not yet been firmly established, though recent works provide some statistical results (Chattopadhyay et al. 2019; Kole et al. 2020). Therefore, we dedicate this work to examining whether any possible connections exist between polarization and jet properties, and aim to confirm the validity of this correlation ($\pi_{\rm KED} \lesssim \pi_{\rm HD} \lesssim \pi_{\rm PED}$) from observations. Practically, several important factors need to be taken into account in our analysis. (i) In order to potentially evaluate all of the frequently-used GRB spectral models and thus diagnose the jet properties, our analysis focuses on the bursts detected by the Gamma-ray Burst Monitor (GBM, 8 KeV-40 MeV, Meegan et al. 2009) onboard the NASA *Fermi* Gamma-ray Space Telescope. (ii) To directly compare the spectral and polarization properties and thus make our results more trustworthy, we select the bursts during which polarization observations and spectral data are available during the same epoch. (iii) Realistically, systematic error is frequently at play in polarization measurements and different polarization instruments have different systematic errors. Therefore, a high-significance signal from polarization measurement is required. In this paper, we collect a sample of the *Fermi*-GBM detected bursts along with the polarized measurements reported in the literature using the time-integrated spectral and polarization analysis approach based on their statistical results, aiming to establish a connection between the polarization and jet properties of GRBs.

The paper is organized as follows. The sample and Methodology are presented in Section 2 and Section 3, respectively. Our results and their physical implication are summarized in Section 4 and Section 5, respectively. The conclusion is presented in Section 5. Throughout the paper, the standard Λ-CDM cosmology with the parameters $H_0 = 67.4$ kms^{-1} Mpc^{-1}, $\Omega_M = 0.315$, and $\Omega_\Lambda = 0.685$ are adopted (Planck Collaboration et al. 2018).

[3] Polarization measurement is a measurement where π ranges from 0% to 100% ($0\% \leq \pi \leq 100\%$) and includes the non-detection (0%), so measuring something consistent with zero is a measurement. Polarization detection, however, indicates a different meaning, where $0\% < \pi \leq 100\%$ and excludes 0%, since we have excluded part of the parameter space equivalent to detection measurements due to the fact that a non-detection of flux implies that we did not measure something.

2 THE SAMPLE

A comprehensive database of GRB polarimetric observations has been created in a recent work (Li et al. 2022a) by extensively searching for those GRBs in the literature whose polarization measurements have been reported. A total of 73 bursts with polarization detections were included in the database, covering a broad wavelength range from radio to optical, X-ray, and γ-ray emission (see Table 1 in Li et al. 2022a). The prompt emission data of these bursts were observed by different satellites (*Fermi*, *Swift*, BeppoSAX, and BATSE). On the other hand, the diagnosis of jet composition usually requires a refined spectral analysis. Among these satellites, *Fermi* covers the broadest energy range in the observation. Consequently, in order to fully evaluate all current spectral models we pay special attention to these *Fermi*-detected bursts. The Gamma-ray Burst Monitor (GBM, 8 KeV-40 MeV, Meegan et al. 2009) and the Large Area Telescope (LAT, 20 MeV- 300 GeV, Atwood et al. 2009), onboard the NASA *Fermi* Gamma-ray Space Telescope, together provide unprecedented spectral coverage for seven orders of magnitude in energy (from $\sim$8 keV to $\sim$300 GeV). Our statistical analysis in the current work includes the prompt γ-ray emission spectral analysis and the connection between the spectrum and polarization are thus based on the *Fermi*-detected bursts. On the other hand, we focus on the GRBs whose polarization measurements were recorded during the prompt emission in the γ-ray band in order to compare the polarization and spectral properties during the same time period. Following are the specific observational properties of the five fascinating bursts (see Table 1) that made up the smaller sample as a result of these selection criteria.

- GRB 100826A. On August 26, 2010 at 22:58:22.898 (T_0) UT, GRB 100826A, was detected by the *Fermi*/GBM. A t_{90} of (84.993$\pm$0.724) s in the 10-1000 keV was measured using the GBM data. The GBM lightcurve exhibits a complicated shape with multiple-peak pulses, and the fluence (flux integrated over the burst duration) in the energy range of 10-1000 keV during the t_{90} duration reported by the GBM team is $(1.6388\pm0.001)\times10^{-4}$ erg cm^{-2} (Figure 2). This burst has no redshift measurement, a value of 2.3 is estimated using the Yonetoku correlation (Yonetoku et al. 2004). Therefore, the isotropic-equivalent energy released from gamma-ray emission in the cosmological frame for this burst can be calculated as, $E_{\gamma,\rm iso}=(3.39^{+0.36}_{-0.33})\times10^{54}$ erg. The KED-to-PFD transition pattern belonging to the "HD" jet type is diagnosed for this burst by using a low-energy spectrum based on a detailed time-resolved spectral analysis during prompt emission (see Section 4). Yonetoku et al. (2011a) reported that a relatively higher polarization degree ($\pi_{\rm obs}$=27$\pm$11) with a 2.9σ linear polarization signal significance was detected during the prompt emission (0-100 seconds after the trigger) of GRB 100826A using a GAmma-ray Polarimeter (GAP) on board a small Japanese solar-power-sail demonstrator, Interplanetary Kite-craft Accelerated by Radiation of the Sun (IKAROS).
- GRB 110301A. On March 01, 2011 at 05:08:43.070 (T_0) UT, GRB 110301A, was detected by the *Fermi*-GBM. A t_{90} of (5.693$\pm$ 0.362) s in the 10-1000 keV was measured using the GBM data. The lightcurve exhibits a complicated shape with multiple-peak pulses, and the fluence in the energy range of 10-1000 keV from T_0+0 s to T_0+5.693 s reported by the GBM team is $(3.5891\pm0.003)\times10^{-5}$ erg cm^{-2} (Figure 3). This burst has no redshift measurement, a value of 0.36 is estimated by using the Yonetoku relation (Yonetoku et al. 2004). With this estimated value of redshift, the isotropic-equivalent energy released from gamma-ray emission in the cosmological frame for this burst can be calculated as, $E_{\gamma,\rm iso}=1.4\times10^{52}$ erg. A KED-to-PFD jet is diagnosed for this burst by using a low-energy

spectrum based on a detailed time-resolved spectral analysis during prompt emission. A linear polarization signal (3.7σ) with a very high polarization degree (π=70$\pm$22) for this burst was claimed by Yonetoku et al. (2012b) using the IKAROS/GAP data 0-7 seconds after the trigger (Figure 3).

• GRB 110721A. On July 21, 2011 at 04:47:43.761 (T_0) UT, GRB 110721A, was detected by the *Fermi*-GBM. A t_{90} of (21.822$\pm$0.572) s in the 10-1000 keV was measured using the GBM data. The lightcurve exhibits a single-peak pulse, and the fluence in the energy range of 10-1000 keV from T_0+0 s to T_0+21.822 s as reported by the GBM team is (3.5891$\pm$0.003)$\times10^{-5}$ erg cm^{-2} (Figure 4). This burst has a value of 0.382 of redshift. With this redshift, we calculate the isotropic-equivalent energy released from gamma-ray emission in the cosmological frame for this burst, $E_{\gamma,\rm iso}$=3.0$\times10^{52}$ erg. A peak-KED jet is diagnosed for this burst by using a low-energy spectrum based on a detailed time-resolved spectral analysis during prompt emission. A linear polarization signal (3.3σ) with a very high polarization degree ($\pi=85^{+16}_{-22}$) for this burst was claimed by Yonetoku et al. (2012b) using the IKAROS/GAP data 0-11 seconds after the trigger (Figure 4).

• GRB 140206A. On 6 February 2014 at 06:36:12.843 UT (T_0), a long burst, GRB 140206B, was detected by *Fermi*-GBM and several other satellites (e.g., INTEGRAL/IBIS). Its GBM lightcurve in the 10-900 keV exhibits three clearly separated emission episodes (G1, G2, and G3) as shown in the left panel of Figure 5, with T_{90} of 146.690$\pm$4.419 s was measured by GBM data. GRB 140206B is a very bright burst, and the fluence (flux integrated over the burst duration) in the energy range of 10-1000 keV from T_0+0 s to T_0+146.690 s reported by the GBM team is (1.23$\pm$0.003)$\times10^{-4}$ erg cm^{-2}. This burst has a value of 2.73 for redshift. With this redshift, we calculate the isotropic-equivalent energy released from gamma-ray emission in the cosmological frame for this burst, $E_{\gamma,\rm iso}$=2.3$\times10^{54}$ erg. The spectral analysis has been performed in great detail in Li (2019a), and three different spectral components (KED-to-PFD) have been identified, a short-thermalized precursor early on, followed up with the main burst with a non-thermal emission later on, and in the last with a fainter burst with still a non-thermal emission. Interestingly, immediately following up with the short-thermalized precursor, a clear polarization signal with 90% confidence was observed 4-26 seconds after the trigger as reported in Götz et al. (2014) using the INTEGRAL/IBIS data. This signal is a linear polarization with an up-limit polarization degree of $\pi > 28$ observed in the γ-ray energy band (Figure 5).

• GRB 160802A. GRB 160802A was detected by GBM on August 2, 2016 at UT 06:13:29.63. A T_{90} of (16.384$\pm$0.362) s in the 10-1000 keV was measured using the GBM data. The prompt emission light curve shows two clearly separated active periods, with a quiescent time interval between the two periods of about 10 seconds. The earlier period consists of overlapping pulses while the latter period shows a clear single-peak pulse. The fluence in the energy range of 10-1000 keV from T_0+0 s to T_0+21.822 s as reported by the GBM team is (6.8399$\pm$0.0057)$\times10^{-5}$ erg cm^{-2}. This burst has no redshift measurement, a value of 0.36 is estimated by using the Yonetoku relation (Yonetoku et al. 2004). Using this estimated value of redshift, we further calculate the isotropic-equivalent energy released from gamma-ray emission in the cosmological frame for this burst, $E_{\gamma,\rm iso}$=2.2$\times10^{53}$ erg. A peak-KED jet for each period is diagnosed for this burst by using a low-energy spectrum based on a detailed time-resolved spectral analysis during prompt emission. A linear polarization signal ($\sim3\sigma$) with a very high polarization degree (π=85$\pm$29) for this burst was claimed by Yonetoku et al. (2012b) using the AstroSat/GZTI data 0-20.34 seconds after the trigger (Figure 6).

3 METHODOLOGY

3.1 Spectral Analysis Techniques

In order to diagnose the jet properties for a given burst, a detailed time-integrated or time-resolved spectral analysis is required. The spectral analysis is performed by a pure Python package, namely, `the Multi-Mission Maximum Likelihood Framework` (`3ML`,Vianello et al. 2015). Moreover, a Bayesian approach and Markov Chain Monte Carlo (MCMC) iterations to explore the best parameter space was used. Our spectral analysis includes the following main steps. (1). First is to select detectors, sources, and background intervals; (2). Second, we used the Bayesian block method (BBlocks, Scargle et al. 2013) to bin the Time-Tagged Events (TTE) lightcurve of the brightest detector (with the minimum viewing angle), and the significance (S, Vianello 2018) for each BBlocks time bin was also calculated. (3). Third, we use a typical GRB spectral model (Band function, Band et al. 1993) to fit all the spectra selected by the BBlocks method and the best model parameters are obtained by adopting a fully Bayesian approach. For a detailed Bayesian spectral analysis and the reduction procedure applied to a GRB spectrum, we refer to Li (2019a,b, 2020); Li et al. (2021); Li & Zhang (2021).

3.2 Using the Yonetoku correlation to infer their redshift values

In order to study the intrinsic properties in the cosmological rest frame, a redshift measurement for each burst is needed. Unfortunately, we currently have 3 bursts (GRB 100826A, GRB 110301A, and GRB 160802A) without known redshift. Several works to infer redshifts using empirical relations of GRB have been reported in the literature(Amati et al. 2002; Yonetoku et al. 2004). For example, (Yonetoku et al. 2004) discovered a new and much tighter relationship between the spectral peak energy ($E_{\rm p}$) and the peak luminosity ($L_{\rm p}$) using the combined data detected by the BeppoSAX and BATSE satellites, and claimed that one can use the $E_{\rm p}$-$L_{\rm p}$ relation to estimating redshift without knowing distances in the BSTASE catalog. We, therefore, attempt applying the Yonetoku relation(Yonetoku et al. 2004) to estimate redshift values for these bursts.

Our procedure to estimate the pseudo-redshift using the Yonetoku relation includes the following steps.

First, we perform a spectral fit to the peak spectrum (the brightest time bin was selected by using the Bayesian blocks method(Scargle et al. 2013) at the highest statistical significance S) of each burst. The peak flux F_γ and peak energy $E_{\rm p}$ on the observer's frame from the spectral fits are thus obtained, where F_γ is the observed peak flux integrated between (1-10^4) keV in units or erg cm^{-2} s^{-1}.

Second, in order to use the $E_{\rm p,z}$-$L_{\rm p,iso}$ relation, a bolometric luminosity in a common cosmological rest-frame energy band (1-10^4 keV) is needed. It can be obtained by using the spectral parameters to conduct a k-correction extrapolating the observed energy band to 1-10^4 keV. For a given burst, the k-correction factor (k_c) can be derived using the following procedure. The observed flux $F^{\rm obs}$ (erg cm^{-2} s^{-1}), in a fixed detector energy bandwidth [e_1, e_2] (for instance, for the *Fermi*-GBM observation, e_1=8 keV, e_2=40 MeV), can be written as:

$$F^{obs}_{[e_1,e_2]} = \int_{e_1}^{e_2} EN(E)dE, \quad (1)$$

where E is in units of keV, and $N(E)$ is a GRB photon number spectrum. The total luminosity emitted in the bandwidth $[e_1,e_2]$, defined in the cosmological rest-frame, is given by:

$$L_{[e_1(1+z),e_2(1+z)]} = 4\hat{\pi}D_L^2(z)F^{\rm obs}_{[e_1,e_2]}, \quad (2)$$

which $D_L(z)$ is the luminosity distance. To express the luminosity L in the cosmological rest-frame energy band, [E_1=1 keV, E_2 =10^4 keV], common to all sources, the Eq.(2) can be rewritten as:

$$L_{[E_1,E_2]} = 4\hat{\pi}D_L^2F^{\rm obs}_{\left[\frac{E_1}{1+z},\frac{E_2}{1+z}\right]} = 4\pi D_L^2k[e_1,e_2,E_1,E_2,z]F^{\rm obs}_{[e_1,e_2]}, \quad (3)$$

where the k-correction factor, k_c, is therefore defined as:

$$k_c = k[e_1,e_2,E_1,E_2,z] = \frac{F^{\rm obs}_{\left[\frac{E_1}{1+z},\frac{E_2}{1+z}\right]}}{F^{\rm obs}_{[e_1,e_2]}} = \frac{\int_{E_1/(1+z)}^{E_2/(1+z)} EN(E)dE}{\int_{e_1}^{e_2} EN(E)dE}, \quad (4)$$

Last, with the k-correction factors known, the peak luminosity can be derived from the observed γ-ray flux F_γ according to $L = 4\hat{\pi}d_L^2F_\gamma k_c$, where d_L is the luminosity distance.

Finally, as long as the prompt emission spectral properties can be obtained, the Yonetoku relation can be used to infer redshift. With the above Steps, one can use Equation (2) in Yonetoku et al. (2004) to estimate their redshift values,

$$\frac{L_{\rm p}}{10^{52}{\rm ergs}^{-1}} = (2.34^{+2.29}_{-1.76}) \times 10^5 \left[\frac{E_{\rm p}(1+z)}{1{\rm keV}}\right]^{2.0\pm0.2}. \quad (5)$$

Table 2 lists the spectral properties obtained from the peak spectral analysis and the estimated redshift values inferred from the Yonetoku relation.

4 RESULTS

4.1 Spectral Properties and their inferred jet properties

Five bursts were claimed to have a high-significance polarization detection (Table 1) and GBM data (Table 4) taken at their prompt emission, thereby providing an "ideal" sample to study the possible connection between jet properties and polarization straightforwardly.

In practice, either time-integrated or time-resolved spectral analysis is frequently used to diagnose their jet properties. Several methods have been widely used to diagnose the jet properties based on their spectral analysis. The simplest method is to use the low-energy spectrum (e.g., Preece et al. 1998) to resolve the jet properties for a given pulse/burst (Method-I). In this method, a single empirical model (such as the Band model) based on a time-resolved technique is typically used. The KED jets, therefore, can be defined as *all* α indices, within uncertainties, in a given burst, obtained from time-resolved spectral analysis, are systematically above the synchrotron limit throughout the entire burst/pulse duration, being consistent with a matter-dominated fireball jet. The PFD jets, on the other hand, are consistent with the scenario that *all* α indices, within uncertainties, in a given burst are below the synchrotron limit throughout the burst/pulse duration, this suggests a Poynting-flux-dominated jet. The HD jets represent the moderate scenario, and can be presented that *some* α indices, obtained from time-resolved spectral analysis, are above the synchrotron limit (α >2/3) while *some* others are below the synchrotron limit (α <2/3) throughout the burst/pulse duration. The HD jets can be further divided into two subcategories. (1) the peak-KED pattern since the thermal emission component (the spectra that violate the LOD line) is only detected around the peak of the pulse (thermal component dominates the peak of a pulse/burst); and (2) the KED-to-PFD (thermal to non-thermal component) transition pattern (Li 2019a), since the thermal emission component is detected at the beginning of the burst, and followed by non-thermal emission component. However, it may be difficult to classify jets as either KED or PFD jets based on the spectral index alone. In contrast to an optically-thin synchrotron emission, a photospheric quasi-thermal component would, in fact, have a harder low-energy spectral index, but this does not guarantee that the jet is KED (Gill et al. 2020). Therefore, a more reliable approach is to find the best model (Method-II) by comparing various frequently-used spectral models using certain statistical information criteria, such as the Akaike Information Criteria (AIC; Akaike 1974), Bayesian Information Criteria (BIC; Schwarz 1978), and the Deviance Information Criterion (DIC; Spiegelhalter et al. 2002; Moreno et al. 2013). After the identification of the best spectral model, one can assess the jet properties using the spectral properties inferred from the best model. Moreover, we may also directly fit the spectral data with a physical model (such as the synchrotron emission model, Burgess et al. 2020; Method-III), so as to diagnose the jet properties and any potential connection with their polarization properties. Our analysis in this task incorporates both Method-I and Method-II (primary method). Method III will be used elsewhere.

We first perform time-integrated spectral analysis (treating the entire epoch of polarization observation as one time bin) by using various GRB spectral models, including power-law (PL), blackbody (BB), cutoff power law (CPL), Band function, PL+BB, CPL+BB, and Band+BB, respectively. We adopted both AIC and BIC to evaluate different spectral models and select the preferred one, and the preferred model is the one that provides the lowest AIC and BIC scores. As such, we define

- PFD jets: a single non-thermal (Band-like) spectral component was found in the time-integrated spectral analysis, like GRB 080916C (Abdo et al. 2009).
- KED jets: a dominate thermal (BB-like) spectral component was found in the time-integrated spectral analysis, like GRB 090902B (Ryde et al. 2010) and GRB 220426A (Deng et al. 2022).
- HD jets: a hybrid spectrum of thermal (BB-like) and non-thermal (Band-like) components was observed in the time-integrated spectral analysis in a single burst, like GRB 110721A (Axelsson et al. 2012), and GRB 140206A (e.g., Li 2019a).

Our refined time-integrated spectral analysis suggests that the Band+BB model can best characterize the spectral shape of all the five bursts (see Table 3). The global properties of our sample used in the spectral analysis are reported in Table 4. These include the GRB name (column 1), observed duration T_{90} of burst[4] (column 2), 10-1000 KeV fluence (column 3), together with the used detectors (column 4), the selected source (column 5) and background (column 6) intervals, and the best model (column 7). The best-fit spectral parameters of the sample with the Band+BB model are reported in Table 5, including GRB name (column 1), source duration (column 2), and corresponding significance (column 3), and Band component normalization K (column 4), low-energy power-law index α (column 5), peak energy $E_{\rm p}$ (column 6) of the νF_ν spectrum, and high-energy power-law index β (column 7); and BB component normalization K (column 8), and temperature kT (column 9).

We next perform time-resolved spectral analysis (treating the entire epoch of polarization observation as divided into multiple-

[4] The time interval during which 90% of the total observed counts have been detected.

time events) for each individual BBlocks time bin using the Band model. Temporal evolution of α is presented in Figures 2-6 for GRB 110826A, GRB 110301A, GRB110721A, GRB 140206A, and GRB 160802A, respectively. With the BBlock time bins selected and the corresponding significance (S) values calculated, the data points are shown in different S ranges[5]: $S < 10$, $10 \leq S \leq 20$, and $S > 20$. For a subset of GRBs, a mixture of thermal (blackbody contribution from the photosphere emission) and non-thermal (synchrotron emission from relativistic electrons) components was observed in a single burst (e.g., Li 2019a). Previous studies (e.g., Burgess et al. 2014) showed that the characteristic energy ($E_{\rm p}$) of non-thermal emission is correlated to the characteristic energy (kT) of thermal emission with a power-law relation in form of $E_{\rm p} \propto T^q$, where q ranges from $\sim$1-2. Burgess et al. (2014) studied a set of bright *Fermi* single-pulse GRBs and claimed that one can use this correlation to identify whether the jet is dominated by kinetic ($q \sim 1$) or magnetic energy ($q \sim 2$) depending on the value of the exponent. GRB 110721A was identified as the baryonic jet type in Burgess et al. (2014) with $q = 1.24 \pm 0.11$, which is also consistent with our finding in the current analysis.

Our time-integrated spectral analysis indicates that *all* five bursts belong to the HD jet type. This finding is quite interesting since only a subset of GRBs (a fairly low percentage) have an observed thermal component in their spectral analysis, as suggested by several statistical studies (e.g., Li 2022a). Recently, (Li 2022a) has made a great effort to collect a complete GRB sample in which all bursts were detected by *Fermi*/GBM with known redshift, and created a spectral parameter catalog based on their model-wise properties. He discovered that $\sim$ 5% (7/153) of the analyzed bursts were found to require a subdominant thermal component in their time-integrated spectral analysis, including GRB 110721A. Our results imply that high-degree polarization measurements may also be associated with a thermal component originating from photosphere emission. Our time-resolved spectral analysis, on the other hand, further suggests that two bursts exhibit the peak-KED pattern (GRB 110721A and GRB 160802A) while the other three bursts (GRB 110301A, GRB 140206A, and GRB 160625B) display the KED-to-PFD transition pattern across the entire burst durations since all α indices are above the synchrotron limit early on ($\alpha >$2/3), and then drop below the synchrotron limit later on ($\alpha <$2/3), indicating a thermal-to-nonthermal transition signature. Interestingly, after carrying out a detailed time-resolved spectral analysis for a sample of the multi-pulsed bursts, Li (2019a) reported that the jet properties for a good fraction of the multi-pulsed bursts exhibit a transition from thermal to non-thermal component among pulses within a single burst, and claimed that such "transition" jet properties are clearly observed in four bursts (GRB 140206B, GRB 140329B, GRB 150330A, and GRB 160625B), and the polarization properties in those transition bursts would also differ.

4.2 The Observed Parameter Correlations: Polarization Degrees versus Other Relevant Quantities

The most interesting result that draws our attention is that all five bursts in our target sample have a relatively high-degree polarization measurement and are associated with the "HD" jet properties. In the following discussion, we, therefore, pay special attention to this interesting observation and its theoretical interpretation.

[5] Note that the results obtained for those lower-S spectra may not be robust, since the spectral fits would not be well determined due to lack of enough photons.

Much evidence points towards the fact that correlation analysis plays a crucial role in the understanding of GRB physics as it provides a crucial clue to revealing its nature (e.g., Amati et al. 2002; Yonetoku et al. 2004; Liang & Zhang 2005; Dainotti et al. 2008; Xu & Huang 2012; Zhang et al. 2012; Liang et al. 2015; Dainotti & Amati 2018; Li 2022a, and references therein). Here, an attempt has been made to explore the correlations between the polarization properties and several typical GRB observed quantities. For instance, the polarization degrees π correlated with (i) the cosmological rest-frame peak energy ($E_{\rm p,z}$) of the νF_ν prompt emission spectrum, (ii) the isotropic-bolometric-equivalent emission energy $E_{\gamma,\rm iso}$, (iii) the magnetization parameter σ_0, (iv) the blackbody temperature kT, (v) the redshift z, and (vi) the corresponding energy fluence S_γ. Using the same observed epoch during the prompt emission phase, our target sample allows for a reasonable comparison. Our analysis includes the following steps. (1) For a given burst in our target sample, we first select the same time interval for the prompt emission data as for the polarization measurement. (2) We then attempt to perform a spectral fit to the selected prompt emission data using PL, BB, CPL, Band, PL+BB, CPL+BB, and Band+BB functions, respectively. The Band+BB model has an AIC/BIC-statistic improvement of at least 10 with respect to the Band-alone and other models for these bursts, which suggests Band+BB as the preferred model that would fit the data and a thermal component existing in the spectrum. Since the thermal flux ratio ($F_{\rm BB}/F_{\rm tot}$) for these bursts is less than 50% (see Table 5), the thermal components thus are subdominant. Interestingly, Chattopadhyay et al. (2019) analyzed the prompt emission and polarization data of 11 bright bursts detected during the first year of operation of CZTI, and reported that of these bursts, four bursts (GRB 160106A, GRB 160509A, GRB 160802A, and GRB 160910A) in their spectral analysis showed a deviation from the Band model and an additional thermal blackbody is needed in order to model their spectrum more precisely. (3) With the spectral analysis done in Step (2), we are able to obtain the spectral peak energy ($E_{\rm p,z}$) and the blackbody temperature (kT). $E_{\gamma,\rm iso}$ can also be calculated in the cosmological frame with a redshift known (GRB 110721A and GRB 140206B), and with a k-correction applied by integrating the observed energy spectrum over 1 KeV/(1+z) to 10 MeV/(1+z). We note here that for the remaining three bursts (GRB 100826A, GRB 110301A, and GRB 160802A) with an unknown redshift, we use the Yonetoku relation (Yonetoku et al. 2004) to estimate their redshift values (see Section 3.2). Using these hybrid-spectrum observed properties and following the method described in Gao & Zhang (2015) and Li (2020), we also calculate the magnetization parameter σ_0 for these bursts. Finally, with these Steps completed, we therefore present π-$E_{\rm p,z}$ (Fig.7a), π-$E_{\gamma,\rm iso}$ (Fig.7b), π-kT_z (Fig.7c), π-σ_0 (Fig.7d), π-z (Fig.7e), and π-S_γ (Fig.7f) plots in Figure 7. Interestingly, these scatter plots all seem to exhibit a monotonic power-law decay in their log-log space (except for the π-σ_0 correlation), with a similar decay slope ranging from -0.40 to -0.20. Our results indicate that a higher $E_{\rm p,z}$, $E_{\gamma,\rm iso}$, and kT_z tend to have a lower-degree polarization π. However, we should note that the sample size is too small to be reliable enough to support the derived conclusion, so the results may not be statistically significant.

5 PHYSICAL IMPLICATION

There are several parameters to impact on the degree of polarization in GRBs including the geometry of the jet, its angular structure, the bulk Lorentz factor of outflow material, the magnetic field configuration and observer's point of view. Here, we consider an

ultra-relativistic axi-symmetric jet which lunched by a central engine weather a black hole or an rapidly rotating magnetar (e.g., Usov 1992; Thompson 1994; Dai & Lu 1998; Wheeler et al. 2000; Zhang & Mészáros 2001; Liu et al. 2007; Metzger et al. 2008; Lei et al. 2009; Metzger et al. 2011; Bucciantini et al. 2012; Lü & Zhang 2014; Li et al. 2018). During the prompt emission, we have ultra-relativistic jet with bulk lorentz factor $\Gamma \gg 1$ leading to strong beaming effect of GRB outflow materials where the Doppler factor can be approximated as

$$\delta_D \approx \frac{2\Gamma}{1+(\Gamma\tilde{\theta})^2}, \tag{6}$$

Due to the relativistic beaming effect of GRB jets, the measured radiation energy of the bursts is smaller than its isotropic energy as $E_\gamma = f_b E_{\gamma,iso}$ by a factor $f_b = \Delta\Omega/4\pi = (1-\cos\theta_j) \approx \theta_j^2/2$ where θ_j is the half opening angle of the ejecta. In principle, different GRBs can be viewed from different observing angles θ_{obs} with respect to the jet's central axis. Only those observers whose line-of-sight (LOS) intersects the surface of the jet can detect the GRBs. In the ultra-relativistic regime, the observed emission mainly receives from a region that is limited to a cone with angular size $\tilde{\theta} \lesssim 1/\Gamma$ around LOS. At the early time prompt emission when the LOS intersects the jet surface, if $\theta_{obs}/\theta_j \lesssim 1-(\Gamma\theta_j)^{-1}$ and $\Gamma\theta_j \gtrsim \mathcal{O}(10)$, the jet's edge remains invisible to the observer Gill et al. (2018).

In this case, the emission region can be approximated as an expanding thin spherical shell of width $\Delta \ll R/\Gamma^2$ (in the lab frame) in which particles cool relatively fast compared to the dynamical time scale of the system. As the GRB jet has slowed down significantly when the opening angle $\theta_j \simeq \Gamma^{-1}$ then the jet break happens and the edge effects become important. The flux density measured by a distant observer from each fluid element in an infinite thin-shell approximation for the prompt emission is given by (Granot 2005)

$$F_\nu(t) = \frac{(1+z)}{16\pi^2 d_L^2(z)} \int \delta_D^3 L'_{\nu'}(r) d\tilde{\Omega}, \tag{7}$$

where $d_L(z)$ is the luminosity distance of the source, and $d\tilde{\Omega} = d\tilde{\phi}d(\cos\tilde{\theta})$ is the solid angle with $\tilde{\theta}$ and $\tilde{\phi}$ as the polar angle and the azimuthal angle measured from the LOS, respectively. The comoving spectral luminosity $L'_{\nu'}(r)$ for the synchrotron emission is

$$L'_{\nu'}(r) = L'_{\nu'}(R)\left[1-(\hat{n}'\cdot\hat{B}')^2\right]^{\frac{1+\alpha}{2}}, \tag{8}$$

where $\alpha = -d\log(F_\nu)/d\log(\nu)$ is the spectral index, $\hat{n}$ is the observer's LOS in the comoving frame of the GRB jet and $\hat{B}$ is the local direction of the magnetic field. The spectral luminosity $L'_{\nu'}(R)$ in the comoving frame of the fluid in terms of frequency ν' and the peak frequency ν'_p at which the most of the power is emitted is given by

$$L'_{\nu'}(R) = L'_{\nu'_p}\left(\frac{\nu'}{\nu'_p}\right)^{-\alpha}, \tag{9}$$

here we consider a constant luminosity with a radius which the peak value $L'_{\nu'_p}$. We assume to have synchrotron emission from accelerating electrons in the magnetig field with isotropic velocity distribution and the energy distribution as a power law $n_e \propto \gamma^{-p}$.

In our scenario, we assume that each pulse originates from a single thin shell and Γ can in principle change for different pulses. The state of polarization of a radiation field can be expressed in terms of the Stokes parameters I (intensity), Q and U (linear polarizations), V (circular polarization). In spite of linear polization, only a few mechanisms can generate the high value of circular polarization in the usual scattering processes in GRBs, and the measured circular polarization has only been reported once in a GRB afterglow Wiersema et al. (2014). Therefore we will not consider circular polarization in this paper. Stokes parameters Q and U are differences in flux for two orthogonal directions on the sky which are coordinate dependent quantities (Rybicki & Lightman 2008; Westfold 1959), we define the local degree of linear polarization $\Pi = \sqrt{Q^2+U^2}/I$ where

$$\frac{U}{I} = \Pi\sin 2\theta_p\,, \qquad \frac{Q}{I} = \Pi\cos 2\theta_p\,, \qquad \theta_p = \frac{1}{2}\arctan\left(\frac{U}{Q}\right)\,, \tag{10}$$

and θ_p is the polarization position angle (PA). The direction of the polarization vector in the synchrotron emission is orthogonal to the LOS of the observer $\hat{n}$ and the local direction of the magnetic field $\hat{B}$ in the jet,

$$\hat{\Pi} = \frac{(\hat{n}\times\hat{B})}{|\hat{n}\times\hat{B})|}, \tag{11}$$

The polarization measurements can help in order to probe the magnetic field structure inside the shock wave. Moreover, the degree of the polarization depends on the GRB jet's angular structure and the observer's viewing angle from jet symmetry axis (Lazzati et al. 2004). The magnetic field structure in KED and PFD flows has a different origin and can be classified into three categories (Gill et al. 2018; Gill et al. 2021): (i) a locally ordered magnetic field ($B_{\rm ord}$) with angular coherent length $\theta_j > \theta_B \gtrsim 1/\Gamma$, (ii) a toroidal magnetic field ($B_{\rm trod}$) which has an ordered axisymmetric configuration in the transverse direction with respect to the jet (iii) a tangent magnetic field which could be in principle parallel ($B_\parallel$) or perpendicular ($B_\perp$) to the local fluid velocity. In the PFD the magnetic field is dynamically dominated and usually has a large coherence length such as $B_{\rm trod}$ which can be produced by a rotating central engine or in a high magnetized flow, other locally and globally ordered field configuration are also possible in this case. On the other hand in KED we may have a tangled magnetic field structure with $B_\perp$ or/and $B_\parallel$ components, however generating such an anisotropic field configurations in shock waves seems to be challenging (Gill & Granot 2020). A globally ordered magnetic field may naturally be advected from near the central source, while the random magnetic fields generated in the shock dissipation region (Kumar & Zhang 2015; Geng et al. 2018; Gill et al. 2018; Fan et al. 2008). The magnetic field structures that are generated at relativistic collision-less shocks, due to the two-stream instabilities, are expected to be tangled within the shock plane (Medvedev & Loeb 1999).

The degree of linear polarization generated in the synchrotron emission from an isotropic electron distribution with power-law energy spectrum, and for a given direction of magnetic field is given by (Rybicki & Lightman 2008; Westfold 1959)

$$\Pi^{lin}_{max} = \frac{\alpha+1}{\alpha+5/3} = \frac{p_{\rm eff}+1}{p_{\rm eff}+7/3}, \tag{12}$$

where $p_{\rm eff} = 2\alpha+1$ is the effective power-law index of the electron distribution.

$$p_{\rm eff} = \begin{cases} 2, & \nu_c < \nu < \nu_m, \quad \text{slow cooling} \\ p, & \nu_m < \nu < \nu_c, \quad \text{fast cooling} \\ p+1, & \nu > \max(\nu_c,\nu_m), \quad \text{either fast or slow cooling} \end{cases} \tag{13}$$

and, therefore

$$\Pi^{lin}_{max} = \begin{cases} 9/13, & \nu_c < \nu < \nu_m, \quad \text{fast cooling} \\ \frac{(p+1)}{(p+7/3)}, & \nu_m < \nu < \nu_c, \quad \text{slow cooling} \\ \frac{(p+2)}{(p+10/3)}, & \nu > \max(\nu_c,\nu_m), \text{either fast or slow cooling} \end{cases} \tag{14}$$

This polarization may originate from a very small region (point-like emitter) in which the magnetic field has a specific orientation. Only in the case of ordered magnetic field with the coherence length comparable or larger than the visible surface of the emitting region, the highest value of the polarization Π^{lin}_{max} in Eq. (19) can be generated. The photon index in the Synchrotron radiation is limited to $-1/3 \leqslant \alpha \lesssim 3/2$ which regarding Eq. (19) leads to the maximum degree of polarization $50\% \lesssim \Pi \lesssim 75\%$. In the left panel of Figure (8), we see predicted polarization values using this theoretical model with observed data using our target sample. Here α indices are obtained using the spectral analysis defined in §4. We find that the observed data are well distributed along the line predicted by this model.

In general, the measured polarization is obtained by integrating the local stokes parameters over the flux of the GRB jet as

$$\Pi(t_f) = \frac{Q(\bar{t}_f)}{I(t_f)} = \frac{\int dF_\nu \cos 2\theta_p}{\int dF_\nu}, \tag{15}$$

assuming to have an axisymmetric flow and taking into account symmetry consideration, we see that $\bar{U} = 0$ and consequently the instantaneous total degree of the linear polarization is $\bar{\Pi} = |\bar{Q}|/I$. We perform an integration over the equal time surface (EATS) for a single pulse $\int \bar{Q}(t)dt / \int I(t)dt$ in order to obtain pulse integrated polarization of the prompt emission which leads to

$$\frac{\Pi_{\rm ord}}{\Pi_{max}} = \frac{\int_0^{y_{max}} dy(1+y)^{-2-\alpha} \int d\phi \Lambda(y,\phi) \cos 2\theta_p}{\int_0^{y_{max}} dy(1+y)^{-2-\alpha} \int d\phi \Lambda(y,\phi)}, \tag{16}$$

The above formula is valid for the prompt emission from an ultra-relativistic thin-shell for an on-axis observer ($\theta_{obs} = 0$) where $y_{max} = (\Gamma\theta_{max})^2$ and θ_{max} defined as the maximum angle from LOS Granot (2003a). The factor $\Lambda(y,\phi)$ is an average over the magnetic field orientations in the plane of the ejecta as

$$\Lambda(y,\phi) \equiv \langle (1-(\hat{n}'\cdot\hat{B}')^2)^{\frac{1+\alpha}{2}} \rangle , \tag{17}$$

The polarization angle θ_p and $\Lambda(y,\phi)$ take different forms regarding the configuration of the magnetic field in the plane the GRB jet. In the case of an ordered magnetic field $B_{\rm ord}$ we have :

$$\Lambda_{\rm ord}(y,\phi) \approx \left[(\frac{1-y}{1+y})^2 \cos^2\phi + \sin^2\phi \right]^{\frac{1+\alpha}{2}}, \tag{18}$$

$$\theta_p = \phi + \arctan\left[(\frac{1-y}{1+y}) \cot\phi \right] . \tag{19}$$

The time-integrated linear polarization in the presence of an ordered magnetic field in the plane normal to the jet velocity is plotted as a function of the spectral index in the right panel of Fig. (8). As it is seen the polarization degree increases towards higher values of α and lower values of y_{max} which can cover the observed polarization of GRB 110721A, GRB 160802A, and GRB 110301A. Therefore for a configuration with the globally ordered magnetic field, high values of linear polarization even larger than 50% are obtainable.

The degree of polarization for a magnetic field with locally tangled or random configuration is obtained by averaging over all directions of the local magnetic field within the plane of the shock (Granot & Königl 2003a; Sari 1999; Gruzinov 1999; Nava et al. 2016). The presence of a random magnetic field leads to negligible values of net linear polarization measured by an on-axis observer. In the case of a random field behind the shock wave only if the observer is off-axis and the circular symmetry is broken, non-zero net polarization is measurable. The total linear polarization arising from the whole jet which is subjected to a random field with a direction perpendicular to the jet velocity is given by Granot (2003a)

$$\frac{\Pi_\perp}{\Pi_{max}} = \frac{\int_{y_1}^{y_2} dy(1+y)^{-2-\alpha} \sin[2\Psi_1(y)] \mathcal{G}(y,\alpha)}{\Theta(1-\zeta)\int_0^{y_1} \frac{dy\ \mathcal{H}(y,\alpha)}{(1+y)^{\alpha+2}} + \int_{y_1}^{y_2} dy \frac{dy\ \mathcal{H}(y,\alpha)}{(1+y)^{\alpha+2}} \left(\frac{\pi-\Psi(y)}{\pi}\right)}, \tag{20}$$

where $\Theta(1-\zeta)$ is the Heaviside step-function with $\zeta \equiv \theta_{obs}/\theta_j$ as a parameter to define observer's point of view, and

$$\mathcal{G}(y,\alpha) = \frac{1}{2\pi}\int_0^\pi d\phi \left[\frac{(1-y)^2}{(1+y)^2}\cos^2\phi - \sin^2\phi \right] \left[1 - \frac{4y\cos^2\phi}{(1+y)^2} \right]^{\frac{\alpha-1}{2}}, \tag{21}$$

$$\mathcal{H}(y,\alpha) = \int_0^\pi d\phi \left[1 - \frac{4y\cos^2\phi}{(1+y)^2} \right]^{\frac{1+\alpha}{2}}, \tag{22}$$

$$\cos\Psi(y) = \frac{(1-\zeta^2)y_j - y}{2\zeta\sqrt{yy_j}}. \tag{23}$$

In above expressions $y_{1,2} = (1\mp\zeta)^2 y_j$ and $y_j = (\Gamma\theta_j)^2$. The variation of the linear polarization in the presence of a random field configuration measured by an off-axis observer is displayed in Fig. (9). In the left panel, the spectral indices are selected to be consistent with average values reported in Table (5) for our *target* sample and for $y_j = 10$. In the right panel, y_j is changed while $\alpha = 1$, it is found that the appeared peak has a width in order of $1/\sqrt{y_j}$. From Fig. (9), we see that the polarization degree is limited to small values for $\zeta < 1$ while it is sharply increased for $\zeta \approx 1$ and finally reaches to an asymptotic limit at $\zeta > \mathcal{O}(1)$. It is seen that the Synchrotron radiation with $B_\perp$ can potentially generate wide range of polarization values from low levels to moderate values which cover observed values associated to our sample. In principle, various viewing angles θ_{obs} and different angular structures of the jet affect the measured fluence of GRBs. Note that the fluence significantly decreases for a top-hat jet viewing from outside the jet's sharp edge, so high levels of polarization in off-axis jets may only be obtainable in very close bursts. In fact, the detectibility of GRB polarization needs high-fluence sources and usually, the fluence rapidly drops below the detector threshold for a large off-axis observer.

The time-resolved spectral analysis in §4.1 showed thermal to non-thermal (KED-to-PFD) transitions in our sample where a sub-dominant component of the thermal emission during bursts is observed. Observing hard values of the spectral indices during the bursts can be served as hints that LOS is not highly off-axis, since high latitude emission leads to a softer spectrum Lundman et al. (2013).

As it was reported in §4.2, a correlation between the polarization and the isotropic energy π-$E_{\gamma,\rm iso}$ (Fig.7b) has been observed within our sample, it is worth mentioning that higher polarization values are recorded for closer bursts GRB 110301A (z=0.36), GRB 110721A (z=0.382), GRB 160802A (z=0.90) and lower values for farther sources GRB 140206B (z=2.73) and GRB 100826A (z=2.3) (Fig.7e). The observed fluences of GRB 140206B and GRB 100826A is higher than other sources (see Table. 4 and Fig.7f) and due to their higher redshifts ζ can not obtain large values, however, low values of ζ would be enough to reproduce their measured polarizations.

The local degree of linear polarization for a tangled or random field configuration for a thin ultrarelativistic shell modeling of the prompt emission by assuming $\alpha = 1$ is obtained by averaging over all local magnetic field directions as

$$\Pi^{\rm lin}_{\rm rnd} = \Pi^{lin}_{max} \frac{(b-1)\sin^2\theta_B}{2+(b-1)\sin^2\theta_B} \tag{24}$$

where $b \equiv 2\langle B_{\parallel}^2 \rangle / \langle B_{\perp}^2 \rangle$ denotes the anisotropy of the magnetic field distribution as the ratio of the parallel $B_{\parallel}$ to the perpendicular $B_{\perp}$ components with respects to the shock direction, and θ_B is the angle between the LOS from the observer and the direction of the shock Sari (1999); Gruzinov (1999). In the case of a globally ordered magnetic field configuration aligned with the jet direction ($B \to B_{\parallel}$, $b \to \infty$), Eq. (24) returns back to Eq. (19) and gives the maximum value of the linear polarization.

The polarized emission may also originate from independent magnetic patches with various field orientation Li (2022a) where magnetic patches are locally coherent but distributed randomly in observed emission region. In this case the measured polarization from different patches is estimated as $\Pi = \Pi_{max}/\sqrt{N}$, where N is the number of magnetic patches or equivalently multiple pulses where the coherence length of the magnetic field is as large as the emission region in a single pulse and observed polarization is an average over multiple pulses (Gruzinov & Waxman 1999; Granot & Königl 2003b).

The magnetic field which is generated within IS for KED jets has usually a coherence length much smaller than the angular size of the emission region which causes negligible net polarization. It has been shown that even by taking into account the angular structure of the flow the polarization is limited to $\Pi \lesssim 20\%$ for photospheric emission of a relativistically expanding fireball Ito et al. (2014); Lundman et al. (2014a); Parsotan et al. (2020). The observed high values of the polarization for GRB 110721A and GRB 160802A while they show the peak-KED pattern cannot be explained simply by the sub-photospheric dissipation model based on Comptonisation. Because the multiple scatterings at large optical depths region leads to wash out the directionality of polarization vectors (Lundman et al. 2018b). To explain the strong polarized signals, models invoking dissipation of ordered magnetic field are favored (Lyutikov et al. 2003; Zhang & Yan 2011b; McKinney & Uzdensky 2012). A structured jet photosphere model may also generate polarized photons via Compton scattering but with a different energy-dependence compare to the synchrotron model in the ordered magnetic field (Chang et al. 2014b,a, 2013).

The Jitter radiation emitted by ultra-relativistic electrons accelerating in a small-scale random magnetic field (Medvedev 2000), can also generate a hard energy spectrum with the photon index as high as $\alpha = +0.5$. Due to the random distribution of the magnetic field, jitter radiation is highly symmetric in the electron radiative plane, leading to the vanishing polarization degree for an on-axis observer (Mao & Wang 2013, 2017; Mao et al. 2018). The maximum level of polarization is obtainable when the emitting plane is viewed from the edge on, it can even reach up to 90% (Prosekin et al. 2016). However, for smaller off-axis viewing angles which can yield measurable fluences, jitter radiation causes almost negligible polarization degree. Meanwhile, regardless of the viewing angle the Jitter radiation cannot produce the observed high degree of polarisation close to the spectral peak energy of the jet.

To summarize, polarization features can be explained either by the synchrotron radiation in the ordered/random magnetic field (Granot 2003b; Granot & Königl 2003b; Nakar et al. 2003), the jet structure (Lazzati & Begelman 2009), or the observer's viewing angle with respect to the jet (Lazzati et al. 2004), even in the case of thermal radiation from the jet photosphere (Lundman et al. 2014b). For a hybrid spectrum which include thermal and non-thermal components, we expect to see relatively high values of the polarization in the prompt emission which can be produced by synchrotron emission mechanism in the ordered magnetic field of the jet, and for random field configurations only for off-axis observers (Gill et al. 2021). However, the spectral properties of our target sample demonstrated that off-axis observations specially for the large viewing angle is not the case, and the observed values of the polarization most probably is a hint of the ordered magnetic field originating from the central engine. Since from PFD jets towards HD and KED jets, polarization washout effects are increased gradually due to thermal photons, we would expect that the inequality $\pi_{\rm KED} \lesssim \pi_{\rm HD} \lesssim \pi_{\rm PED}$ is satisfied if other conditions are fixed for a given jet. Due to the different degrees of polarization predicted by different emission models in various energy bands, it is essential to have a high-sensitivity gamma-ray polarimeter with a wide band-pass to detect energy-dependent polarization signals and constrain different models (Zhang 2014). However, it should be noted that due to several free parameters in polarization models, upcoming more precise observations and theoretical investigations are needed to discriminate between competing models in order to explain observed joint polarization and spectral properties.

6 CONCLUSION

Early polarization observations during the prompt emission phase play a crucial role in understanding the radiation mechanism and jet composition of GRBs. Observations over the past few decades suggest that the jet composition of GRBs may have diverse properties. If the jet composition is matter-dominated (i.e., a fireball), the GRB prompt emission spectra would include a bright thermal component originating from the fireball photosphere. Alternatively, if the jet composition is Poynting-flux-dominated, the GRB prompt emission spectra would include a dominant non-thermal component originating from the synchrotron radiation. Moreover, if the jet composition is hybrid-dominated, the GRB prompt emission spectra would include a thermal component originating from the fireball photosphere and a non-thermal component originating from the synchrotron radiation. It is highly speculated that the prompt emission is likely expected to be strongly polarized owing to its non-thermal origin. Consequently, a different level of polarization degrees ($\pi_{\rm KED} \lesssim \pi_{\rm HD} \lesssim \pi_{\rm PED}$) during the prompt emission phase is naturally expected due to the different types of jet composition. In this paper, we have collected a GRB sample in which all the bursts detected by *Fermi*/GBM and whose polarization detection in the emission region was also reported in the literature, containing five interesting bursts (GRB 100826A, GRB 110301A, GRB 110721A, GRB 140206A, and GRB 160802A). Using the time-averaging polarization observations and selecting the same epoch for the GBM data taken during the prompt emission phase, we then attempted to explore the correlations between jet properties and polarization properties of GRBs and aimed to confirm the validity of this correlation ($\pi_{\rm KED} \lesssim \pi_{\rm HD} \lesssim \pi_{\rm PED}$) from observations.

We first performed a detailed time-averaged spectral analysis for each burst in our target sample by using several frequency-used GRB spectral models and selected the best one by using information criteria (AIC and BIC). The jet properties of GRBs can be classified into three categories based on their spectral analysis: the "KED", "PFD", and "HD" types. Using the spectral properties we then inferred their jet properties and discovered that all five bursts belong to the "HD"-jet type. The lack of the other two types of jets (KED and PED) prevents us from validating this correlation ($\pi_{\rm KED} \lesssim \pi_{\rm HD} \lesssim \pi_{\rm PED}$). Hopefully, upcoming instruments will provide high-sensitivity polarization observations in the future, leading to well-sampled, well-studied data sets, enabling such statistical analysis.

We next conducted a time-resolved spectral analysis for each in-

dividual burst by dividing the emission period into multiple-time slices using the BBlocks method using the Band-alone model. Our refined time-resolved spectral analysis, on the other hand, further suggested that the "HD"-type has two subcategories: the peak-KED pattern and the KED-to-PFD transition pattern. In our attempt to assess the jet properties of GRBs using Band-α evolution, we discovered that two bursts exhibit the peak-KED pattern (GRB 110721A and GRB 160802A) whereas the other three bursts show the KED-to-PFD transition pattern (GRB 110301A, GRB 140206A, and GRB 160625B). All five bursts found in the "HD"-type imply that the photosphere emission may also be a possible mechanism to power the high-degree polarization observation.

We also made an attempt to explore the correlations between the polarization properties and several typical GRB observed quantities. Using the same observed epoch during the prompt emission phase, our target sample allows for a reasonable comparison. The correlations we attempted to study included the polarization degrees π correlated with (i) the cosmological rest-frame peak energy ($E_{\rm p,z}$) of the νF_ν prompt emission spectrum, (ii) the isotropic-bolometric-equivalent emission energy $E_{\gamma,\rm iso}$, (iii) the magnetization parameter σ_0, (iv) the blackbody temperature kT, (v) the redshift z, and (vi) the corresponding energy fluence S_γ. As a result, we discovered that a higher $E_{\rm p,z}$, $E_{\gamma,\rm iso}$, and kT_z tend to have a lower-degree polarization π.

Lastly, we discovered that all five bursts in our target sample have a relatively high-degree polarization detection that seems to correlate with the "HD"-jet type. If it is an intrinsic characteristic of GRBs, this could provide a clue to studying the radiation mechanism and jet composition of GRBs. We have also discussed some physical interpretations of this interesting phenomenon. Since the configuration of the magnetic field inside the jet is one of the crucial parameters to determine the polarization degree, we discussed two main configurations (i.e. ordered and random fields), and their connection to the jet composition is clarified. We considered polarization patterns as a function of different dynamical parameters associated to the outflow materials, the spectral indices and the observer's LOS with respect to the jet. Combining the spectral analysis and the polarization measurements allowed us to find out the detection of polarization values $\Pi > 50\%$ during prompt emission of GRB 160802A, GRB 110721A and GRB 110301A is a piece of strong evidence for the synchrotron emission mechanism in the presence of an ordered magnetic field which can be advected from the GRB central engine. Regarding the different properties of our target sample, we conclude that geometrical effects and large off-axis observations are unlikely responsible for the measured polarizations assuming random magnetic fields within the jets.

Finally, there are some caveats that are worth mentioning when applying our analysis. (i) Spectrum. We have resolved the jet properties based on the low-energy spectrum. However, it may be difficult to classify jets as either KED or PFD jets based on the spectral index alone. Indeed, a photospheric quasi-thermal component would have a harder low-energy spectral index as compared to an optically-thin synchrotron, but that does not guarantee that the jet is KED (an example, see Gill et al. 2020). (ii) Polarization. The degree of polarization ultimately probes the (local) structure of the B-field in the emission region. An ordered field would necessarily yield high polarization whereas a tangled field would yield a very small polarization. It is unclear, however, whether these field configurations are exclusive to a given jet configuration (or a particular level of magnetization). In addition, the angular structure of the jet also plays an important role in governing the observed polarization. Thus, due to the large range of model parameters, it is difficult to attribute a given level of polarization to a given jet composition. More discussion is provided in a recent review article (Gill et al. 2021). (iii) Different instrument analysis. Currently, it is not clear why different instruments, namely, POLAR, IKAROS-GAP, and ASTROSAT/CZTI, are finding different levels of polarization for a small sample of GRBs (Chattopadhyay et al. 2019). There is no consensus. POLAR is finding a rather low-level polarization, which is consistent with zero within 3σ of their quoted central values, whereas both IKAROS and AstroSAT are finding much higher levels. Hard X-ray to soft gamma-ray polarization measurements are very tricky and the analysis has to be carried out very carefully. As such, some of these measurements are probably not representative of GRBs and need to be further verified by future more precise instruments. (iv) Time-resolved polarization analysis. In the current analysis, none of the cases have shown time-resolved polarization measurements. Even though the GRBs in our target sample have time-resolved spectral indices, not having corresponding polarization measurements makes it difficult to ascertain the properties of the B-field and outflows.

Acknowledgements. We thank Ramandeep Gill, Jonathan Granot, Rahim Moradi, Mi-Xiang Lan, Asaf Pe'er, Jin-Jun Geng, Christoffer Lundman, Remo Ruffini, and ICRANet members for many discussions on GRBs physics and phenomena. This research made use of the High Energy Astrophysics Science Archive Research Center (HEASARC) Online Service at the NASA/Goddard Space Flight Center (GSFC).

Data availability. The data underlying this article will be shared on reasonable request to the corresponding author.

REFERENCES

Abdo, A. A., Ackermann, M., Arimoto, M., et al. 2009, Science, 323, 1688
Acuner, Z., Ryde, F., Pe'er, A., Mortlock, D., & Ahlgren, B. 2020, ApJ , 893, 128
Acuner, Z., Ryde, F., & Yu, H.-F. 2019, MNRAS , 487, 5508
Akaike, H. 1974, IEEE Transactions on Automatic Control, 19, 716
Amati, L., Frontera, F., Tavani, M., et al. 2002, A&A , 390, 81
Atwood, W. B., Abdo, A. A., Ackermann, M., et al. 2009, ApJ , 697, 1071
Axelsson, M., Baldini, L., Barbiellini, G., et al. 2012, ApJ , 757, L31
Band, D., Matteson, J., Ford, L., et al. 1993, ApJ , 413, 281
Bégué, D., Samuelsson, F., & Pe'er, A. 2022, ApJ , 937, 101
Bucciantini, N., Metzger, B. D., Thompson, T. A., & Quataert, E. 2012, MNRAS , 419, 1537
Burgess, J. M., Bégué, D., Greiner, J., et al. 2020, Nature Astronomy, 4, 174
Burgess, J. M., Preece, R. D., Ryde, F., et al. 2014, ApJ , 784, L43
Chand, V., Chattopadhyay, T., Iyyani, S., et al. 2018, ApJ , 862, 154
Chang, Z., Jiang, Y., & Lin, H. N. 2013, Astrophys. J., 769, 70
Chang, Z., Jiang, Y., & Lin, H.-N. 2014a, Astrophys. J., 780, 68
Chang, Z., Lin, H.-N., & Jiang, Y. 2014b, Astrophys. J., 783, 30
Chattopadhyay, T., Vadawale, S. V., Aarthy, E., et al. 2019, ApJ , 884, 123
Coburn, W., & Boggs, S. E. 2003, Nature , 423, 415
Dai, Z. G., & Lu, T. 1998, A&A , 333, L87
Dai, Z. G., Wang, X. Y., Wu, X. F., & Zhang, B. 2006, Science, 311, 1127
Dainotti, M. G., & Amati, L. 2018, PASP, 130, 051001
Dainotti, M. G., Cardone, V. F., & Capozziello, S. 2008, MNRAS , 391, L79
Deng, L.-T., Lin, D.-B., Zhou, L., et al. 2022, ApJ , 934, L22
Fan, Y.-Z., Xu, D., & Wei, D.-M. 2008, Mon. Not. Roy. Astron. Soc., 387, 92
Gao, H., & Zhang, B. 2015, ApJ , 801, 103
Geng, J.-J., Huang, Y.-F., Wu, X.-F., Song, L.-M., & Zong, H.-S. 2018, Astrophys. J., 862, 115
Geng, J.-J., Huang, Y.-F., Wu, X.-F., Zhang, B., & Zong, H.-S. 2018, ApJS , 234, 3
Gill, R., & Granot, J. 2020, Mon. Not. Roy. Astron. Soc., 491, 5815

Gill, R., Granot, J., & Beniamini, P. 2020, MNRAS , 499, 1356
Gill, R., Granot, J., & Kumar, P. 2018, arXiv:1811.11555
Gill, R., Kole, M., & Granot, J. 2021, Galaxies, 9, 82
Götz, D., Laurent, P., Antier, S., et al. 2014, MNRAS , 444, 2776
Granot, J. 2003, Astrophys. J. Lett., 596, L17
Granot, J. 2003a, ApJ , 596, L17
—. 2003b, ApJ , 596, L17
—. 2005, ApJ , 631, 1022
Granot, J., & Königl, A. 2003a, APJ, 594, L83
—. 2003b, ApJ , 594, L83
Gruzinov, A. 1999, ApJ , 525, L29
Gruzinov, A., & Waxman, E. 1999, Astrophys. J., 511, 852
Guiriec, S., Connaughton, V., Briggs, M. S., et al. 2011, ApJ , 727, L33
Guiriec, S., Kouveliotou, C., Daigne, F., et al. 2015, ApJ , 807, 148
Ito, H., Nagataki, S., Matsumoto, J., et al. 2014, ApJ , 789, 159
Ito, H., Nagataki, S., Matsumoto, J., et al. 2014, Astrophys. J., 789, 159
Kole, M., De Angelis, N., Berlato, F., et al. 2020, A&A , 644, A124
Kumar, P., & Zhang, B. 2015, Phys. Rep. , 561, 1
Lan, M.-X., & Dai, Z.-G. 2020, ApJ , 892, 141
Lan, M.-X., Wang, H.-B., Xu, S., Liu, S., & Wu, X.-F. 2021, Astrophys. J., 909, 184
Lazzati, D., & Begelman, M. C. 2009, ApJ , 700, L141
Lazzati, D., Rossi, E., Ghisellini, G., & Rees, M. J. 2004, MNRAS , 347, L1
Lei, W. H., Wang, D. X., Zhang, L., et al. 2009, ApJ , 700, 1970
Li, L. 2019a, ApJS , 242, 16
—. 2019b, ApJS , 245, 7
—. 2020, ApJ , 894, 100
—. 2022a, arXiv e-prints, arXiv:2211.12187
—. 2022b, ApJ , 941, 27
Li, L., Ryde, F., Pe'er, A., Yu, H.-F., & Acuner, Z. 2021, ApJS , 254, 35
Li, L., Wu, X.-F., Lei, W.-H., et al. 2018, ApJS , 236, 26
Li, L., Xue, S.-S., & Dai, Z.-G. 2022a, arXiv e-prints, arXiv:2208.03583
Li, L., & Zhang, B. 2021, ApJS , 253, 43
Li, L., Geng, J.-J., Meng, Y.-Z., et al. 2019, ApJ , 884, 109
Li, L., Wang, Y., Ryde, F., et al. 2022b, arXiv e-prints, arXiv:2212.02141
Liang, E., & Zhang, B. 2005, ApJ , 633, 611
Liang, E.-W., Lin, T.-T., Lü, J., et al. 2015, ApJ , 813, 116
Liu, T., Gu, W.-M., Xue, L., & Lu, J.-F. 2007, ApJ , 661, 1025
Lloyd, N. M., & Petrosian, V. 2000, ApJ , 543, 722
Lü, H.-J., & Zhang, B. 2014, ApJ , 785, 74
Lundman, C., Pe'er, A., & Ryde, F. 2013, MNRAS , 428, 2430
—. 2014a, MNRAS , 440, 3292
—. 2014b, MNRAS , 440, 3292
Lundman, C., Vurm, I., & Beloborodov, A. M. 2018a, Astrophys. J., 856, 145
—. 2018b, Astrophys. J., 856, 145
Lyutikov, M., Pariev, V. I., & Blandford, R. D. 2003, ApJ , 597, 998
Lyutikov, M., Pariev, V. I., & Blandford, R. D. 2003, Astrophys. J., 597, 998
Mao, J., Covino, S., & Wang, J. 2018, Astrophys. J., 860, 153
Mao, J., & Wang, J. 2013, Astrophys. J., 776, 17
—. 2017, Astrophys. J., 838, 78
McGlynn, S., Clark, D. J., Dean, A. J., et al. 2007, A&A , 466, 895
McKinney, J. C., & Uzdensky, D. A. 2012, MNRAS , 419, 573
Medvedev, M. V. 2000, Astrophys. J., 540, 704
Medvedev, M. V., & Loeb, A. 1999, ApJ , 526, 697
Meegan, C., Lichti, G., Bhat, P. N., et al. 2009, ApJ , 702, 791
Mészáros, P., & Rees, M. J. 2000, ApJ , 530, 292
Metzger, B. D., Giannios, D., Thompson, T. A., Bucciantini, N., & Quataert, E. 2011, MNRAS , 413, 2031
Metzger, B. D., Quataert, E., & Thompson, T. A. 2008, MNRAS , 385, 1455
Moreno, E., Vazquez-Polo, F. J., & Robert, C. P. 2013, arXiv e-prints, arXiv:1310.2905
Nakar, E., Piran, T., & Waxman, E. 2003, J. Cosmology Astropart. Phys., 10, 005
Nava, L., Nakar, E., & Piran, T. 2016, Monthly Notices of the Royal Astronomical Society, 455, 1594
Parsotan, T., Lopez-Camara, D., & Lazzati, D. 2020, Astrophys. J., 896, 139
Pe'er, A. 2015, Advances in Astronomy, 2015, 907321
Pe'er, A., Mészáros, P., & Rees, M. J. 2006, ApJ , 642, 995
Pe'Er, A., & Ryde, F. 2017, International Journal of Modern Physics D, 26, 1730018
Planck Collaboration, Aghanim, N., Akrami, Y., et al. 2018, arXiv e-prints, arXiv:1807.06209
Preece, R. D., Briggs, M. S., Mallozzi, R. S., et al. 1998, ApJ , 506, L23
Prosekin, A. Yu., Kelner, S. R., & Aharonian, F. A. 2016, Phys. Rev., D94, 063010
Rees, M. J., & Meszaros, P. 1994, ApJ , 430, L93
Rees, M. J., & Mészáros, P. 2005, ApJ , 628, 847
Rybicki, G. B., & Lightman, A. P. 1979, Radiative processes in astrophysics
Rybicki, G. B., & Lightman, A. P. 2008, Radiative Processes in Astrophysics (John Wiley & Sons)
Ryde, F., Axelsson, M., Zhang, B. B., et al. 2010, ApJ , 709, L172
Sari, R. 1999, APJ, 524, L43
Scargle, J. D., Norris, J. P., Jackson, B., & Chiang, J. 2013, ApJ , 764, 167
Schwarz, G. 1978, Annals of Statistics, 6, 461
Shakeri, S., & Allahyari, A. 2018, JCAP, 11, 042
Song, X.-Y., Zhang, S.-N., Ge, M.-Y., & Zhang, S. 2022, MNRAS , 517, 2088
Spiegelhalter, D. J., Best, N. G., Carlin, B. P., & Van Der Linde, A. 2002, Journal of the royal statistical society: Series b (statistical methodology), 64, 583
Thompson, C. 1994, MNRAS , 270, 480
Toma, K., Sakamoto, T., Zhang, B., et al. 2009a, ApJ , 698, 1042
—. 2009b, ApJ , 698, 1042
Usov, V. V. 1992, Nature , 357, 472
Vereshchagin, G., Li, L., & Bégué, D. 2022, MNRAS , 512, 4846
Vianello, G. 2018, ApJS , 236, 17
Vianello, G., Lauer, R. J., Younk, P., et al. 2015, arXiv e-prints, arXiv:1507.08343
Wang, Y., Li, L., Moradi, R., & Ruffini, R. 2019, arXiv e-prints, arXiv:1901.07505
Wang, Y., Zheng, T.-C., & Jin, Z.-P. 2022, ApJ , 940, 142
Westfold, K. C. 1959, ApJ , 130, 241
Wheeler, J. C., Yi, I., Höflich, P., & Wang, L. 2000, ApJ , 537, 810
Wiersema, K., Covino, S., Toma, K., et al. 2014, Nature , 509, 201
Willis, D. R., Barlow, E. J., Bird, A. J., et al. 2005, A&A , 439, 245
Xu, M., & Huang, Y. F. 2012, A&A , 538, A134
Yonetoku, D., Murakami, T., Nakamura, T., et al. 2004, ApJ , 609, 935
Yonetoku, D., Murakami, T., Gunji, S., et al. 2011a, ApJ , 743, L30
—. 2011b, ApJ , 743, L30
—. 2012a, ApJ , 758, L1
—. 2012b, ApJ , 758, L1
Zhang, B. 2014, International Journal of Modern Physics D, 23, 1430002
—. 2018, The Physics of Gamma-Ray Bursts, doi:10.1017/9781139226530
Zhang, B., & Mészáros, P. 2001, ApJ , 552, L35
Zhang, B., & Yan, H. 2011a, ApJ , 726, 90
—. 2011b, ApJ , 726, 90
Zhang, F.-W., Shao, L., Yan, J.-Z., & Wei, D.-M. 2012, ApJ , 750, 88
Zhang, S.-N., Kole, M., Bao, T.-W., et al. 2019, Nature Astronomy, arXiv:1901.04207

Table 1 A sample of GRB polarimetric observations

GRB (*Fermi* ID)	PD (π%)	PA ($^\circ$)	Energy band	Time (t-t_0)	Significance (σ)	Instrument	Ref. (For polarization)	z
100826A(957)	27 ± 11	159±18, 75±20	γ-ray	0-100s	2.9σ	IKAROS-GAP	Yonetoku et al. (2011b)	NA
110301A(214)	70 ± 22	73±11	γ-ray	0-7s	3.7σ	IKAROS-GAP	Yonetoku et al. (2012a)	NA
110721A(200)	84^{+16}_{-28}	160±11	γ-ray	0-11s	3.3σ	IKAROS-GAP	Yonetoku et al. (2012a)	0.382
140206A(275)	> 28	80±15	γ-ray	4-26s	90% confidence	INTEGRAL-IBIS	Götz et al. (2014)	2.73
160802A(259)	85±29	$\sim$-32	hard X-rays	0-20.34s	$\sim\mathbf{3}\sigma$	*AstroSat*-CZTI	Chand et al. (2018)	NA

Table 2 Estimated values of redshift using the Yonetoku relation

GRB	$t_{\rm start}\sim t_{\rm stop}$ (s)	S	$E_{\rm p}^{\rm obs}$ (keV)	$F_{\rm p}^{\rm obs}$ (erg cm^{-2} s^{-1})	$k_{\rm c}$	$L_{\rm p}$ (erg s^{-1})	z (Estimated)
100826957	18.208∼22.288	107.97	459±20	$(1.42\pm0.10)\times10^{-5}$	0.85	$(1.27\pm0.10)\times10^{53}$	2.3
110301214	3.876∼4.126	107.60	126±6	$(1.36\pm0.16)\times10^{-5}$	1.02	$(1.46\pm0.17)\times10^{53}$	0.36
160802259	0.962∼1.171	73.79	385±39	$(3.04\pm0.80)\times10^{-5}$	0.95	$(3.05\pm0.80)\times10^{53}$	0.90

Table 3 Comparison of AIC/BIC between the best model and other models

GRB	$t_1 \sim t_2$ (s)	AIC/BIC(1) (PL)	AIC/BIC(2) (BB)	AIC/BIC(3) (CPL)	AIC/BIC(4) (Band)	AIC/BIC(5) (PL+BB)	AIC/BIC(6) (CPL+BB)	AIC/BIC(7) (Band+BB)
100826A(957)	0∼100	11662/11670	12225/12232	6819/6830	6706/6721	7819/7834	6693/6712	6638/6661
110301A(214)	0∼7	10969/10978	20029/20038	5342/5354	5284/5301	6124/6140	5302/5323	5254/5278
110721A(200)	0∼11	7319/7327	14194/14203	5694/5707	5541/5557	7323/7340	5524/5544	5504/5528
140206A(275)	4∼26	12649/12657	20413/20421	7617/7630	7431/7448	8549/8566	7345/7366	7293/7317
160802A(259)	0∼20.34	6840/6847	7480/7487	3984/3994	3898/3912	4383/4397	3839/3856	3840/3861

Table 4 Global properties of the Sample

GRB (*Fermi* ID)	T_{90} (s)	Fluence (erg cm^{-2})	Detectors	$\Delta T_{\rm src}$ (s)	$[\Delta T_{(\rm bkg,1)}, \Delta T_{(\rm bkg,2)}]$ (s)	Spectral model (Preferred)
100826A(957)	84.993±0.724	(1.64±0.01)×10^{-4}	n7(n8)b1	(0 to 100)	(-20 to -10, 200 to 250)	Band+BB
110301A(214)	5.693±0.362	(3.59±0.01)×10^{-5}	n7(n8)nbb1	(0 to 7)	(-20 to -10, 40 to 60)	Band+BB
110721A(200)	21.822±0.572	(3.70±0.01)×10^{-5}	(n6)n7n9b1	(0 to 11)	(-20 to -10, 40 to 60)	Band+BB
140206A(275)	146.690±4.419	(1.23±0.01)×10^{-4}	n0(n1)n3b0	(4 to 26)	(-40 to -20, 70 to 90)	Band+BB
160802A(259)	16.384±0.362	(6.84±0.01)×10^{-5}	(n2)b0	(0 to 20.34)	(-20 to -10, 60 to 80)	Band+BB

Table 5 Spectral Fit Results of the Sample with the Band+BB Model.

GRB	$t_1 \sim t_2$ (s)	S	K (Band) (ph.s^{-1}.cm^{-2}.keV^{-1})	α (Band)	E_p (Band) (keV)	β (Band)	K (BB) (ph.s^{-1}.cm^{-2}.keV^{-1})	kT (BB) (keV)	Flux (erg.cm^{-2}.s^{-1})	Flux ratio (F_{BB}/F_{tot})
100826957	0∼82	102.7	$(3.04^{+0.16}_{-0.16})\times10^{-2}$	$-0.84^{+0.04}_{-0.04}$	518^{+46}_{-46}	$-2.28^{+0.07}_{-0.07}$	$(5.54^{+1.97}_{-1.93})\times10^{-5}$	21^{+2}_{-2}	$(3.20^{+0.34}_{-0.31})\times10^{-6}$	$0.03^{+0.03}_{-0.03}$
110301214	0∼7	276.8	$(3.73^{+0.34}_{-0.30})\times10^{-1}$	$-0.72^{+0.07}_{-0.07}$	114^{+2}_{-3}	$-2.87^{+0.08}_{-0.07}$	$(1.14^{+0.57}_{-0.49})\times10^{-2}$	7^{+1}_{-1}	$(5.90^{+0.73}_{-0.69})\times10^{-6}$	$0.04^{+0.03}_{-0.03}$
110721200	0∼11	114.5	$(3.01^{+0.09}_{-0.09})\times10^{-2}$	$-1.20^{+0.02}_{-0.02}$	1620^{+234}_{-229}	$-2.19^{+0.10}_{-0.10}$	$(1.73^{+0.33}_{-0.34})\times10^{-5}$	33^{+2}_{-2}	$(6.94^{+0.66}_{-0.63})\times10^{-6}$	$0.03^{+0.01}_{-0.01}$
140206275	4∼26	170.2	$(3.87^{+0.11}_{-0.11})\times10^{-2}$	$-1.06^{+0.02}_{-0.02}$	679^{+43}_{-43}	$-2.32^{+0.08}_{-0.08}$	$(4.78^{+0.53}_{-0.52})\times10^{-5}$	27^{+1}_{-1}	$(4.57^{+0.25}_{-0.24})\times10^{-6}$	$0.05^{+0.01}_{-0.01}$
160802259	0∼20.34	151.7	$(3.89^{+0.21}_{-0.21})\times10^{-2}$	$-1.00^{+0.03}_{-0.03}$	515^{+44}_{-44}	$-3.23^{+0.73}_{-0.74}$	$(9.11^{+1.22}_{-1.21})\times10^{-5}$	25^{+1}_{-1}	$(3.85^{+0.55}_{-0.41})\times10^{-6}$	$0.09^{+0.02}_{-0.02}$

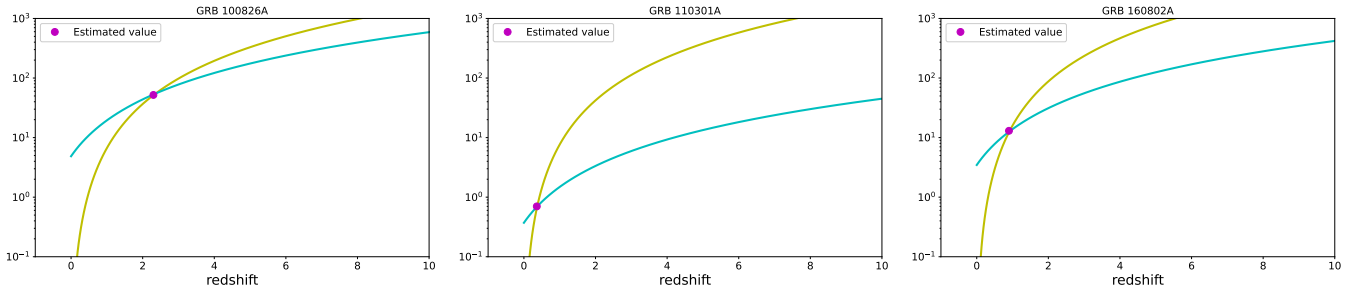


Figure 1. Estimated redshift using the Yonetoku relation for three bursts (GRB 100826A, GRB 110301A, and GRB 160802A). The yellow and cyan lines represent the left and right function of Eq.(5), and their intersection point (purple color) is the estimated value of redshift.

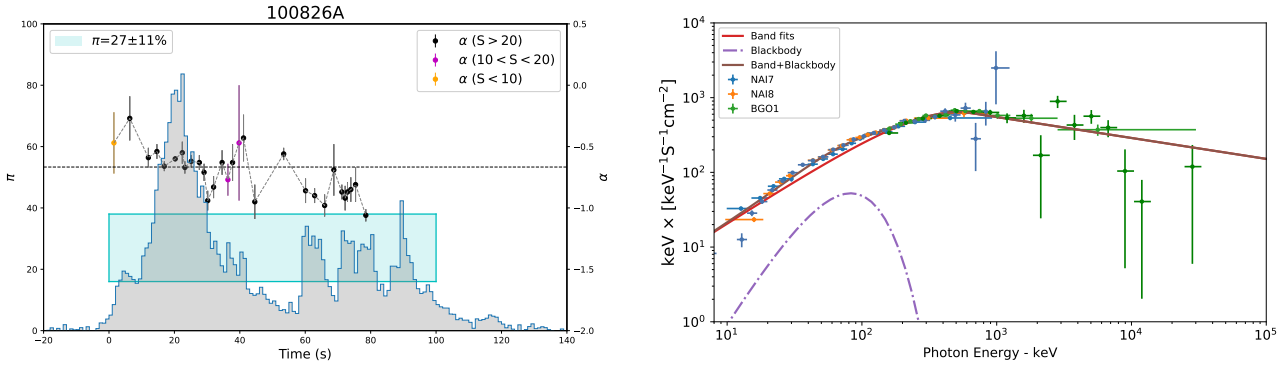


Figure 2. Left panel: prompt emission GBM light curve (overlaid in gray) and polarization observations in γ-ray/hard X-ray energy bands (cyan shaded area), as well as the temporal evolution of α based on the time-resolved spectral analysis. The horizontal dashed line represents the limiting value of $\alpha = -2/3$ for electrons in the slow-cooling regime. Right panel: the spectral data and its best-fit model (Band+BB) during the time epoch (see Table 1 and Table 4) of the matching polarization observations.

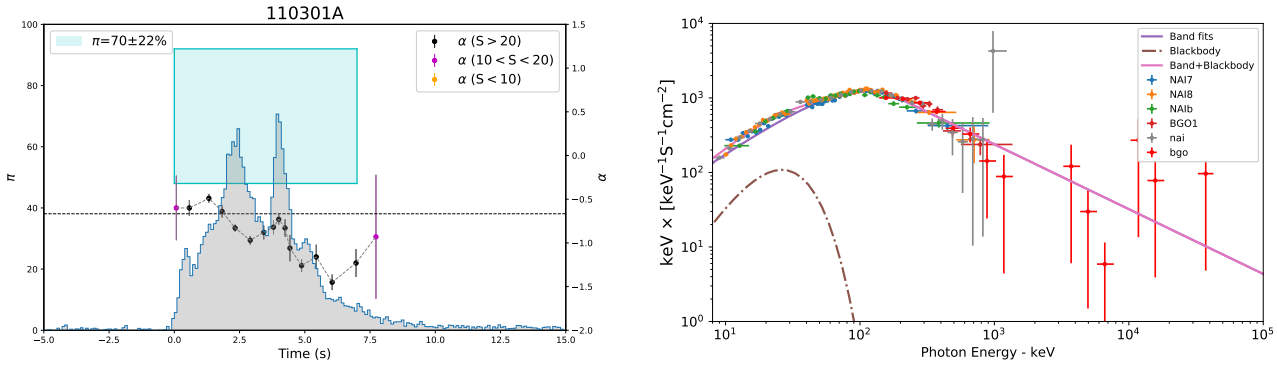


Figure 3. Same as Figure 2 but for GRB 110301A.

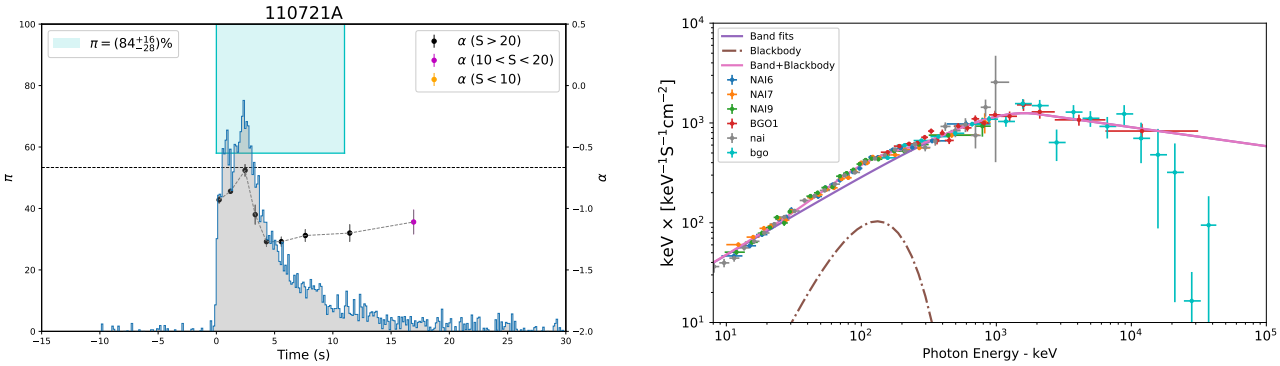


Figure 4. Same as Figure 2 but for GRB 110721A.

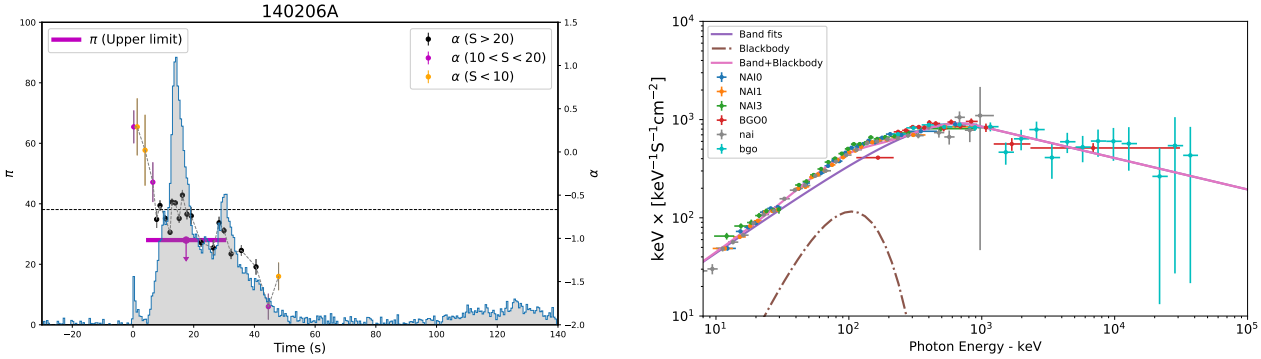


Figure 5. Same as Figure 2 but for GRB 140206A.

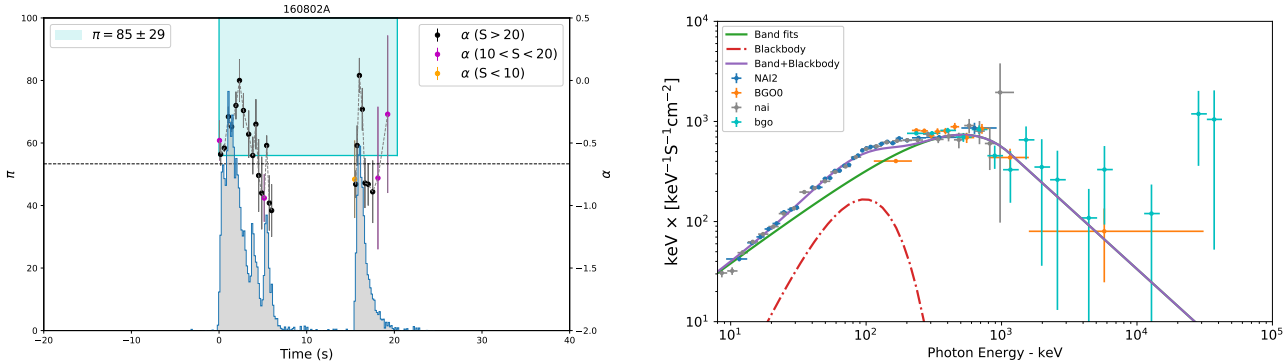


Figure 6. Same as Figure 2 but for GRB 160802A.

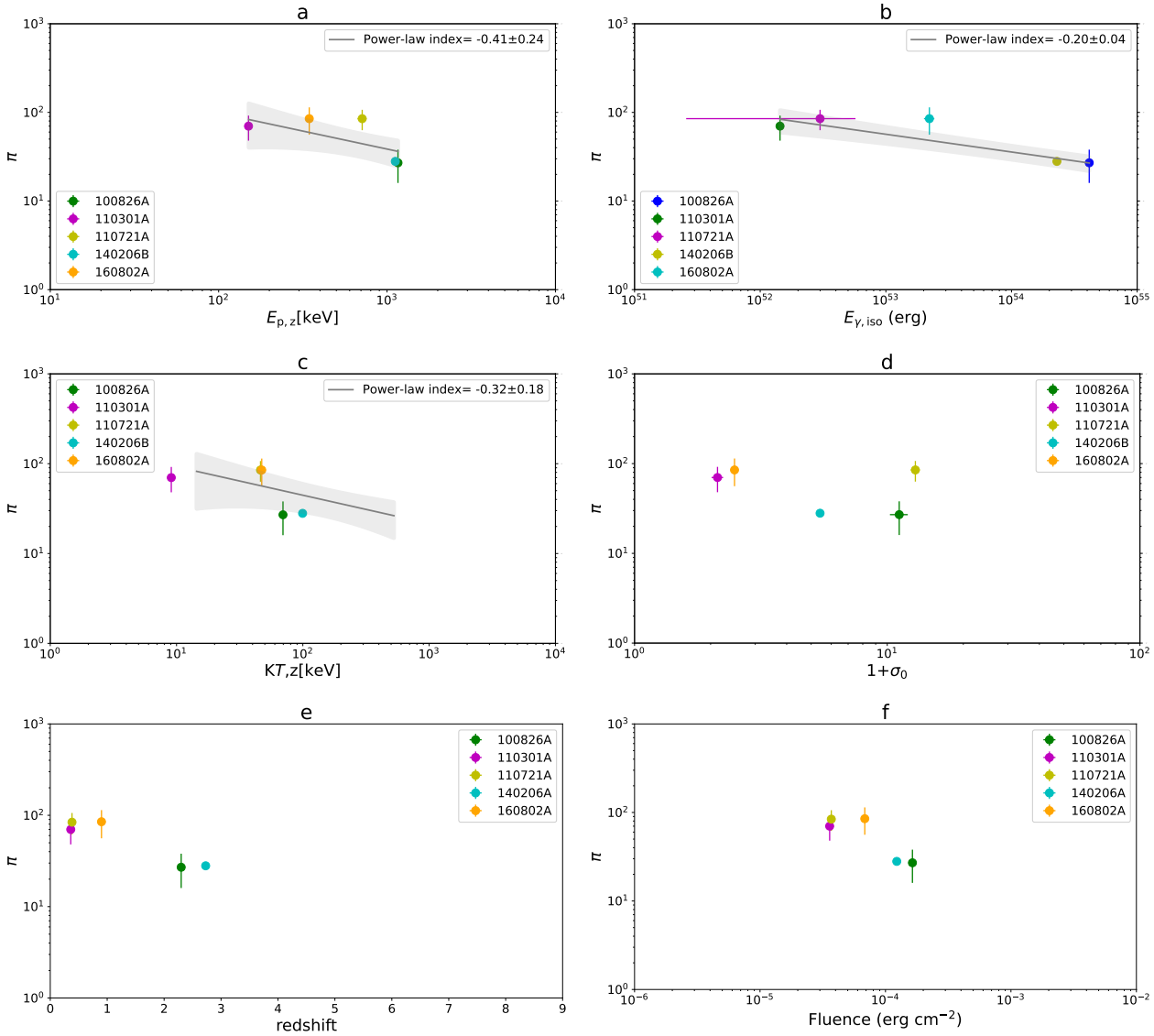


Figure 7. Scatter plots of polarization degree π versus several other observed quantities: (a) the cosmological rest-frame peak energy ($E_{\mathrm{p,z}}$) of the νF_ν prompt emission spectrum, (b) the isotropic-bolometric-equivalent emission energy $E_{\gamma,\mathrm{iso}}$, (c) the magnetization parameter σ_0, (d) the blackbody temperature kT, (e) the redshift z, and (d) the corresponding energy fluence S_γ. Data points with different colors indicate the different bursts in our target sample. The solid lines (grey) are the best fit using the power-law model with 2σ (95% confidence interval) error region (shadow area).

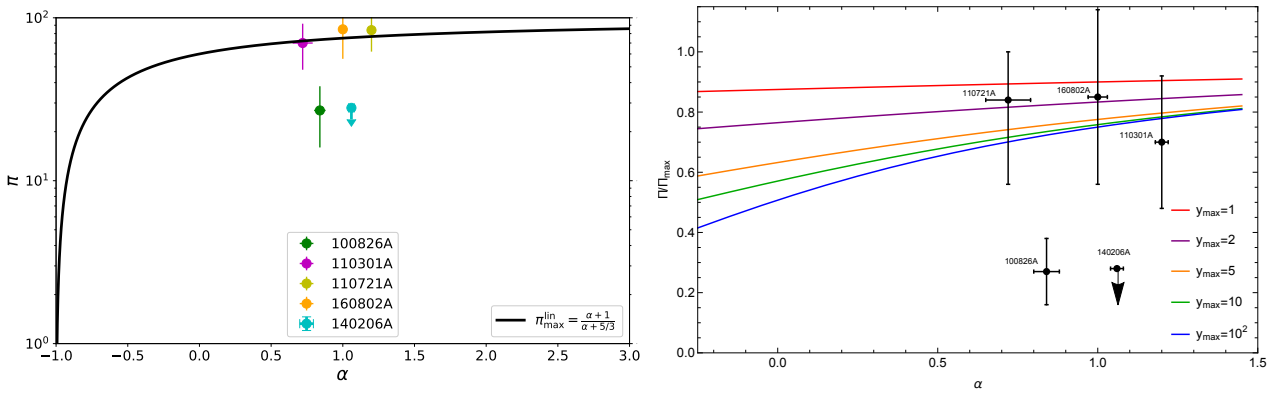


Figure 8. Left: The maximum degree of the linear polarization applying synchrotron emission model ($\Pi^{\rm lin}_{\rm max}$ Eq. (19)) with observed data using α indices based on a time-integrated spectral analysis. Right: Time integrated polarization degree in the presence of an ordered magnetic field $B_{\rm ord}$ with in the plane of ejecta (Eq. (19)) measured by an on-axis observer ($\theta_{obs} = 0$), the evolution of the polarization is plotted in terms of α for different values of $y_{\rm max} = (\Gamma\theta_{\rm max})^2$.

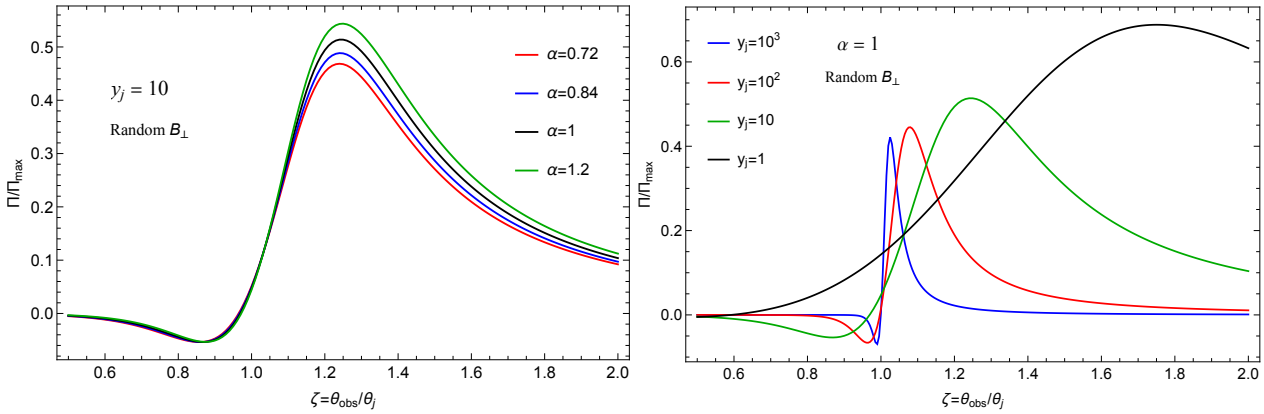


Figure 9. The time integrated polarization for a random magnetic field $B_\perp$ which lies entirely in the plane of the shock (Eq. (20)) as a function of the off-axis parameter $\zeta = \theta_{obs}/\theta_j$ for different values of spectral index α (left) and $y_j = (\Gamma\theta_j)^2$ (right) as labeled.